## University of Bristol - Explore Bristol Research
### General rights

**Key Points:**
- We use tephra from two Holocene lake cores near to Aluto volcano: one contains 24 tephras deposited over 9 kyr and the other 20 over 5.5 kyr
- Glass chemistry is similar for all tephras, and so componentry is used as a correlative tool in combination with trace element data
- Cluster analyses reveal three eruption clusters comprising microlite-rich Vulcanian eruptions separated by larger, microlite-poor eruptions

# Using Lake Sediment Cores to Improve Records of Volcanism at Aluto Volcano in the Main Ethiopian Rift

K. McNamara[1] 📍, K. V. Cashman[1], A. C. Rust[1], K. Fontijn[2] 📍, F. Chalié[3], E. L. Tomlinson[4], and G. Yirgu[5]

[1]School of Earth Sciences, University of Bristol, Bristol, UK, [2]Department of Earth Sciences, University of Oxford, Oxford, UK, [3]Aix-Marseille Université, CNRS, IRD, CEREGE, UM 34, Aix en Provence, France, [4]Department of Geology, Trinity College Dublin, Dublin, Ireland, [5]School of Earth Sciences, University of Addis Ababa, Addis Ababa, Ethiopia

**Abstract** Aluto is a silicic volcano in central Ethiopia, flanked by two large population centers and home to an expanding geothermal power plant. Here we present data from two lake sediment cores sampled 12 and 25 km from the volcano, which record at least 24 distinct eruptions in the Holocene. Tephra layers from the two cores are correlated using a variety of techniques, including major and trace element geochemistry as well as textural and morphological features from scanning electron microscopy-backscatter electron imaging. The purpose is to provide a Holocene reference section for further tephrostratigraphic studies of the volcano as well as to provide information on eruption frequency. The lake cores suggest that Aluto has had a variable eruption rate, with three eruption *clusters* in the Holocene at ~3, 6.5, and 11 ka, with small Vulcanian-to sub-Plinian eruptions separated by larger, Plinian eruptions. We infer that the smaller tephras are likely the product of pumice cone- and dome-forming eruptions. In addition, modern wind data suggest that the likely direction of an ash cloud from Aluto is to the west and south west, which is toward population centers and is in agreement with thickness data from the cores. We conclude that current records underestimate the volcano's eruptive history and that hazard assessments should be updated accordingly.

**Plain Language Summary** In this study we explore the history of a populated volcano in central Ethiopia called Aluto. The volcano is close to several large towns and home to an expanding geothermal power plant. Aluto has not erupted in the last few hundred years, and so there are no eye witness accounts of volcanic activity. In lieu of this, we use volcanic material deposited in the surrounding environment during an eruption as a record of the volcano's activity. In this study, we examine the volcanic material deposited in two lakes using lake cores drilled ~12 and 27 km from the volcano that record the eruptive history from 2,000 to 12,000 years ago. These cores record 24 volcanic eruptions; which indicates an eruption every ~250 years. We use features of the volcanic ash particles to match up eruptions in the cores and to establish when the eruptions occurred. We find that the volcano has had three periods of increased activity, each lasting around 1,000 years. As such, we can infer that the volcano has erupted frequently over the last 10,000 years and hazard assessments of the volcano should be updated accordingly.

## 1. Introduction

A report by Aspinall et al. (2011) that categorized levels of both volcanic hazard and uncertainty ranks 41 of the ~60 volcanoes in Ethiopia at the highest level of uncertainty, 11 of which also have the highest degree of population exposure. Interferometric synthetic aperture radar (InSAR) data show that many of these volcanoes in the Main Ethiopian Rift are actively deforming (Biggs et al., 2011; Hutchison, Fusillo, et al., 2016), some with associated seismicity (Wilks et al., 2017). One of these volcanoes—Aluto—is the target of this study.

Aluto is situated approximately 200 km from Ethiopia's capital city, Addis Ababa. The volcano is flanked by several population centers, including Ziway and Adami Tullu, which in 2007 had populations of ~43,600 and 10,000, respectively (World Bank, 2007). A geothermal plant inside the caldera of the volcano represents significant investment as well as a potentially important source of power for the region.

The risk to local populations and infrastructure underlines the need for additional data on which to build hazard assessments for Aluto volcano. Both the relative inaccessibility and poor terrestrial preservation of the volcanic products present challenges for retrieving details about individual eruptions. Indeed, the Smithsonian Global Volcanism Programme lists only one (poorly documented) Holocene eruption of Aluto around 2,000 years ago. More recent studies indicate, in contrast, eruptive activity as recently as ~400 year BP and at an average rate of an eruption every ~300 years (Fontijn et al., 2018; Hutchison, Pyle, et al., 2016).
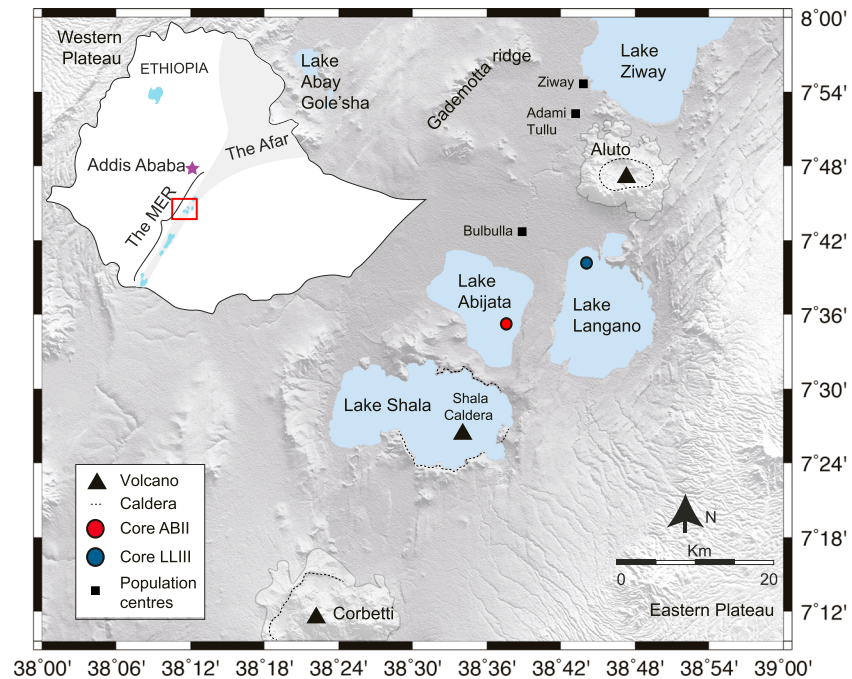
**Figure 1.** Map of Aluto and surrounding area and its location in Ethiopia. Red circle indicates location of core ABII taken from lake Abijata (Chalié & Gasse, 2002). Blue circle indicates location of core LLIII taken from lake Langano (Gibert et al., 2002). MER = Main Ethiopian Rift.

Together, the recent signs of active deformation and seismicity, and the evidence of frequent eruptive activity, motivate our volcanological study of the Holocene tephra record.

Aluto forms part of the Main Ethiopian Rift, a continental rift system bounded by faults on either side of a central plateau running from the northeast to the southwest of Ethiopia (e.g., Mohr, 1971; Ebinger & Casey, 2001; Corti, 2009; Figure 1). Scoria cones and basaltic lava flows dominate (although are not limited to) the rift margins, while larger silicic centers, such as Aluto, punctuate the rift axis (e.g., Abebe et al., 2007; Corti, 2009; Keir et al., 2015; WoldeGabriel et al., 1990). The central volcanoes have erupted a range of compositions that include basalts and trachytes, although peralkaline rhyolites are most common (Fontijn et al., 2018; Hutchison, Fusillo, et al., 2016; Hutchison, Pyle, et al., 2016; Mohr & Wood, 1976; Rooney et al., 2005). Most of these centers experienced mid-Pleistocene caldera-forming eruptions followed by lower magnitude events, some of which have extended into the Holocene (Hutchison, Pyle, et al., 2016). Aluto and its most proximal volcanic neighbors, Shala and Corbetti, have all undergone such caldera-forming eruptions (Di Paola, 1972; Hutchison, Biggs, et al., 2016; Mohr et al., 1980).

Shala caldera (approximately 40 km south of Aluto) has experienced limited postcaldera activity, with the possible exception of scoria cones to the south of the caldera (Fontijn et al., 2018; Mohr, 1971; Trua et al., 1999). There is also evidence of lower-magnitude postcaldera activity at the Tullu Fike complex immediately north of the caldera, which may be the source of late Quaternary pumice deposits located in the caldera walls (Fontijn et al., 2018; Mohr et al., 1980). In contrast, Corbetti, approximately 80 km south of Aluto, has ongoing seismicity and deformation that appear related to magmatic activity (e.g., Biggs et al., 2011; Lloyd et al., 2018). It has produced several silicic Holocene eruptions, which have generated aphyric obsidian flows and/or pumice fall deposits and are documented in terrestrial sections and lake sediment cores up to 167 km from the volcano (Fontijn et al., 2018; Martin-Jones et al., 2017; Rapprich et al., 2016).

Aluto has erupted predominantly peralkaline rhyolites of pantelleritic composition, although initial trachytic flows began around 500 ka and preceded one, or possibly two, rhyolitic caldera-forming eruptions at ~306 to 316 ka (Hutchison, Biggs, et al., 2016). There is little evidence of activity after this period, suggesting a possible hiatus until an eruption at ~55 ka of localized obsidian flows within the caldera and pumice cone-building events, the size, and frequency of which are not well constrained (Hutchison, Biggs, et al., 2016).

Geophysical studies using magnetotellurics combined with well and core log data suggest that the shallow magmatic system at Aluto comprises a complex locked crystal mush below a geothermal reservoir (Gianelli & Teklemariam, 1993; Samrock et al., 2015; Teklemariam et al., 1996). Combining these data with InSAR and soil $CO_2$ measurements suggests the hydrothermal system is fed by a (~4-km deep) magma reservoir which degasses via the geothermal reservoir in the upper 2 km of the volcano (Hutchison, Fusillo, et al., 2016). From this perspective, recent signals of inflation and subsidence (Biggs et al., 2011) may record cycles of fresh magma supply (causing inflation) followed by degassing (causing deflation).

There is only limited published information on the Holocene eruptive history except for descriptions of tephras in terrestrial sections on the edifice and to the west of the volcano where deep gorges expose Holocene-Pleistocene lacustrine sediments. A subset of these tephra deposits was chemically analyzed and correlated by Fontijn et al. (2018), who proposed an initial Holocene tephrostratigraphic framework for the volcano. Holocene pyroclastic deposits are also present in more distal gorges and lake cores (Benvenuti et al., 2002; Chalié & Gasse, 2002; Gasse & Street, 1978; Gibert et al., 2002; Le Turdu et al., 1999) as well as in sediment cores from two lakes close to Aluto: Lake Abijata (Chalié & Gasse, 2002), and Lake Langano (Gibert et al., 2002). The timing, thickness, and chemical composition of tephra layers in the cores has not been previously documented.

The Lake Abijata core (ABII) was drilled approximately 25 km southwest of Aluto (Figure 1). Chalié and Gasse (2002) report eight pyroclastic layers and four layers of *coarse sand* in the core log. Twelve $^{14}$C dates were obtained from organic material sampled at regular intervals along the core, and indicate sediment deposition from ~0.2 to 11.4 cal. ka BP (Gibert et al., 1999), with pyroclastic layers present between ~4 and 12 cal. ka BP.

The Langano core (LLIII) was drilled ~12 km south of Aluto; here Gibert et al. (2002) describe *air-fall pyroclastic layers* 1- to 3-cm thick at 960 and 820-cm depth, indicating *recent explosive volcanic activity*. Additional pyroclastic layers are noted at 532–537 cm, 385–390 cm, 348–352.5 cm, and 139–150 cm although there are no further descriptions of the material. Six $^{14}$C dates indicate a sediment record from ~5.1 to 12.7 cal. ka BP, with volcanic material observed between ~5.6 and 11 cal. ka BP (Gibert et al., 2002).

While limited in detail, the lake core descriptions provide tantalizing evidence for multiple Holocene eruptions of the volcano, consistent with assessment of the terrestrial sections. Here we characterize and correlate individual tephra layers in the two cores using both physical and chemical signatures, with the goal of establishing a robust Holocene stratigraphy. This stratigraphy can be used as a reference for further tephrostratigraphic study of the volcano and the wider region and to inform hazard assessment. At the same time, observations of tephra grain size and componentry provide important information on the range of eruption styles responsible for these tephra layers.

## 1.1. Uses of Tephrostratigraphy

Correlating tephras is common in volcanology, archeology and paleoclimatology (e.g., Fontijn et al., 2016; Lowe, 2011; Tryon et al., 2008; Vogel et al., 2010) and is most often used to determine isochronous features for dating sequences. In many cases, however, the value of the tephra layers for physical volcanology is overlooked. The primary correlation tool is geochemistry, including major and trace element concentrations in volcanic glass (e.g., Lowe, 2011). In more proximal settings, this is sometimes complemented by mineral chemistry (e.g., Smith et al., 2011)—particularly Fe-Ti oxides—which, where present, can help to identify the volcanic source (e.g., Fierstein, 2007; Rawson et al., 2015; Shane et al., 1998). Similarity coefficients and other numerical correlation techniques can be used to relate the glass composition of chemically similar tephras from a large data set (e.g., Brendryen et al., 2010; Kuehn & Foit, 2006). Critically, the success of geochemical correlation techniques relies on an individual eruption producing chemically homogenous samples. Identifying different eruptions from the same volcano is also predicated on the existence of chemically distinct samples within a large well-constrained data set.

Lithological descriptions of ash particles have been used to supplement geochemical data when the chemical variation is insufficient to correlate the tephras, or where more information is required about eruption dynamics. For example, glass shard shape can be used to fingerprint eruptions, where shape is analyzed qualitatively and categorized using a binocular microscope (Placzek et al., 2009; Shane & Smith, 2000). Alternatively, the 2-D external shape of particles can be characterized using quantitative shape parameters (Cioni et al., 2008; Dellino & La Volpe, 1996; Liu et al., 2015, 2016; Wei et al., 2003). Grain size data and

tephra thickness data can also be integrated into the data set to constrain the eruption size (e.g., Wulf et al., 2004).

Physical volcanology studies of tephra deposits aim to constrain eruption conditions using measurements of deposit thickness, and particle size, shape, and density. These studies use isopachs (contours of constant thickness or mass) and isopleths (contours of constant grain size, either maximum or median) to infer eruption magnitude and intensity (e.g., Bonadonna & Houghton, 2005; Carey & Sparks, 1986; Fierstein & Nathenson, 1992; Legros, 2000; Pyle, 1989). Where there are only limited tephra sites, however, such methods are difficult to employ, particularly when a robust stratigraphic framework is not available.

### 1.2. Using Tephra to Constrain Eruption Processes

Textural studies of tephra deposits are more limited but demonstrate the use of textures—grain size, shape, and components—to infer conditions of magma storage, ascent, and eruption (e.g., Cashman & McConnell, 2005; Liu et al., 2015, 2017; Wright et al., 2012), as well as the extent of secondary modification of pumice populations (e.g., Buckland et al., 2018; Jones et al., 2016). Specifically, internal bubble and crystal textures can be calibrated using decompression experiments to identify the existence and extent of conduit-filling plugs, (Cashman, 2004; Clarke et al., 2007; Wright et al., 2012), to infer rates of magma ascent (Klug & Cashman, 1994; Wright et al., 2012), and to measure progressive abrasion in pyroclastic density currents (e.g., Buckland et al., 2018; Jones et al., 2016). External shapes of ash particles provide information on fragmentation conditions (e.g., Cioni et al., 2014; Liu et al., 2015, 2017). Only rarely have ash groundmass textures been used in combination with glass componentry to fingerprint deposits (e.g., Cioni et al., 2008; Di Roberto et al., 2018).

An important consideration in tephrostratigraphy is the variation in tephra components with distance from the vent. Lapilli and coarse ash particles typically fall singly at a rate determined by the terminal velocity, which is a function of particle size, shape, and density (Bonadonna et al., 1998). For this reason, the proportion of different tephra components will vary when they have different settling velocities, depending on the eruption size, distance from the vent and the ash dispersion axis (e.g., Bursik, 1996; Cashman & Rust, 2016; Hildreth & Drake, 1992). This velocity sorting is responsible for crystal concentration zones (Scarpati et al., 2014) and distal enrichment in vitric components, particularly highly vesicular and/or platy glass shards (Liu et al., 2017).

Tephra components also vary with eruption style. Sustained high-intensity explosive (Plinian) eruptions produce high proportions of glass shards (e.g., Cashman & Rust, 2016; Rose & Chesner, 1987). This is because the magma ascent, and associated decompression-induced degassing, is too rapid to allow syneruptive crystallization of microlites, except in hydrous mafic magmas. The result is a deposit dominated by microlite-free glass shards (Geschwind & Rutherford, 1995; Hammer et al., 1999; Swanson et al., 1989). Pulsatory sub-Plinian or Vulcanian eruption styles, in contrast, are characterized by intereruptive development of dense conduit-filling plugs or domes. Associated degassing (e.g., Hammer et al., 1999) drives rapid shallow crystallization and associated microlite-rich glass (Cashman & McConnell, 2005; Clarke et al., 2007). In these conditions, the abundance and geometry of microlites can provide information on magma ascent rate, as well as plug thickness and location (Blundy & Cashman, 2001; Miwa et al., 2013; Noguchi et al., 2006; Szramek et al., 2006; Wright et al., 2012). For this reason, the presence of both microlite-free and microlite-bearing glass within the same deposit provides good evidence for Vulcanian/sub-Plinian eruption styles (e.g., Blundy & Cashman, 2001; Cashman & McConnell, 2005; Melnik & Sparks, 1999; Sparks, 1997).

In this study, we use analyses of tephra layers from the lake sediment cores near Aluto to constrain the chemical and physical characteristics of the layers. Using these characteristics, we correlate the tephras between the cores and make initial interpretations about eruption frequency, size and style.

## 2. Methods

Tephra layers in the lake sediment cores were sampled in May 2015. All cores had been kept sealed since they were retrieved in 1999 from Lakes Abijata (core ABII) and Langano (core LLIII). Every visible tephra was sampled across the entire layer, and most layers thicker than 4–5 cm were subsampled. This equates to 25 different tephra layers in ABII (five of which were subsampled) and 20 in LLIII (two of which were subsampled; Table 1).

**Table 1**

*Summary of Tephra Layers Sampled in Cores ABII, Cored From Lake Abijata, and LLIII, Cored From Lake Langano Table Includes a Description of Each Tephra Layer, the Position in the Core, Tephra Thickness, OxCal Modeled Age, and a Summary of the Analyses Performed on Each Layer*

| Sample | Description | Depth (cm) | Thickness (cm) | Md φ | Minimum Oxcal age (cal. years BP) | Maximum Oxcal age (cal. years BP) | Grain size | SEM | Componentry | EPMA | LA-ICP-MS |
|---|---|---|---|---|---|---|---|---|---|---|---|
| ABII | | | | | | | | | | | |
| ABII-04-14 | Very fine laminated sediment | 314 | <1 | 4.2 | 2423 | 3320 | X | — | [a] | X | — |
| ABII-04-17 | Beige fine-grained laminated sediment | 317 | 2 | 5.0 | 2460 | 3329 | X | X | X | — | — |
| ABII-04-33 | Beige fine-grained laminated sediment | 333 | <1 | 4.8 | 2754 | 3399 | X | [a] | [a] | — | — |
| ABII-04-40 | Beige fine-grained laminated sediment | 340 | <1 | 4.2 | 2958 | 3439 | X | [a] | [a] | — | — |
| ABII-04-62 | Normally graded ash | 362 | 11 | 1.8 | 3167 | 3612 | X | X | X | — | — |
| ABII-04-67 | deposit. A thin fine ash | | | 0.7 | | | X | X | X | X | |
| ABII-04-73 | layer at the base, then fining upward | | | 1.7 | | | X | X | X | | |
| ABII-05-48 | Whiteish fine ash | 447 | 3 | 4.8 | 3608 | 3972 | X | X | X | X | - |
| ABII-05-55 | Light gray/white very fine ash | 455 | <1 | 5.8 | 3614 | 4025 | X | X | [a] | [a] | — |
| ABII-05-60 | Light gray, fine ash | 458 | 8 | 4.2 | 3631 | 4066 | X | X | — | X | — |
| ABII-06-77 | Light gray, very fine ash | 574 | 6 | 4.5 | 4266 | 5037 | X | X | X | — | — |
| ABII-06-88 | Not well preserved, dark gray ash | 587 | 3 | 4.4 | 4318 | 5141 | X | X | [a] | [a] | — |
| ABII-08-16 | Darker gray, very fine ash | 695 | 3 | 4.2 | 5412 | 5980 | X | X | X | X | — |
| ABII-08-46 | Medium gray fine ash | 726 | 3 | 3.9 | 5555 | 6158 | X | X | X | X | — |
| ABII-08-76 | Gray, normally | 756 | 4 | 5.9 | 5677 | 6294 | X | X | X | — | — |
| ABII-08-78 | graded ash | | | 1.5 | | | X | X | X | X | |
| ABII-08-79 | | | | 3.9 | | | X | — | — | — | |
| ABII-09-03 | Gray, medium-grained ash | 773 | 2 | 0.9 | 5771 | 6509 | X | X | X | X | X |
| ABII-09-08 | Lighter gray, medium-fine ash | 779 | 3 | −2.2 | 5799 | 6540 | X | X | X | X | X |
| ABII-09-31 | Very light gray, medium ash | 800 | 4 | 3.7 | 6005 | 6803 | X | X | X | X | — |
| ABII-10-45 | Pumice lapilli in dark gray mud | 915 | <1 | −2.0 | 7979 | 8844 | X | X | [a] | X | — |
| ABII-10-73 | Normally graded | 943 | 5 | 3.33 | 8542 | 9426 | X | X | X | — | — |
| ABII-10-75 | lapilli layer, mixed | | | 0.15 | | | X | X | X | X | X |
| ABII-10-77 | white and gray ash | | | 0.14 | | | X | X | X | X | — |
| ABII-11-07 | Light gray, medium ash | 976 | 4 | 3.9 | 9186 | 10150 | X | X | X | X | — |
| ABII-11-62 | Medium to coarse dark | 1031 | 4 | 4.6 | 10680 | 10128 | X | — | — | — | — |
| ABII-11-64 | gray ash at the base, light gray/white finer ash at the top | | | 4.2 | | | X | X | X | X | |
| ABII-11-79 | Normally graded ash | 1048 | 4 | 6.5 | 10235 | 11118 | X | — | — | — | — |
| ABII-11-81 | layer, darker at base | | | 4.6 | | | X | X | X | X | X |
| ABII-12-11 | Medium to light gray fine ash | 1075 | 3 | 4.8 | 10427 | 11582 | X | X | X | X | — |
| ABII-12-16 | Medium to light gray fine ash | 1080 | 3 | 3.9 | 10452 | 11597 | X | X | X | X | — |
| ABII-12-24 | Dark gray, medium-coarse ash and light gray lapilli | 1089 | 2 | 1.3 | 10525 | 11681 | X | X | X | X | — |
| ABII-12-69 | Medium gray, medium to fine ash | 1134 | 2 | 4.9 | 11258 | 12466 | X | X | X | — | — |
| LLIII | | | | | | | | | | | |
| LLIII-03-01 | Fine lapillli in gray mud | 222 | 1 | 0.9 | 5195 | 5938 | X | X | — | X | — |
| LLIII-03-70 | Dark gray, coarse ash | 292 | 1 | 0.9 | 5545 | 6516 | X | X | X | X | X |
| LLIII-03-110 | Dark gray coarse ash to lapilli | 331 | 1 | 1.2 | 5885 | 6827 | X | X | X | X | X |

**Table 1** *(continued)*

| Sample | Description | Depth (cm) | Thickness (cm) | Md ϕ | Minimum Oxcal age (cal. years BP) | Maximum Oxcal age (cal. years BP) | Grain size | SEM | Componentry | EPMA | LA-ICP-MS |
|---|---|---|---|---|---|---|---|---|---|---|---|
| LLIII-04-11 | Fine ash with scattered lapilli | 346 | 2 | 5.3 | 6034 | 6906 | X | X | — | — | — |
| LLIII-04-18 | Fine gray ash | 348 | 6.5 | 4.5 | 6045 | 6916 | X | X | — | — | — |
| LLIII-04-51 | Medium gray ash | 385 | 5 | 4.4 | 6567 | 7151 | X | X | X | X | — |
| LLIII-05-23 | Gray medium ash | 470 | 5 | 3.5 | 6782 | 8132 | X | X | X | X | — |
| LLIII-05-106 | Lapilli | 556 | <1 | 1.4 | 6979 | 8929 | X | — | — | — | — |
| LLIII-07-75 | Medium gray ash | 752.5 | 4.5 | 0.0 | 9003 | 10565 | X | X | X | X | X |
| LLIII-07-105 | Gray lapilli | 782 | 2 | 3.3 | 9324 | 10669 | X | X | X | X | — |
| LLIII-08-38 | Gray medium to fine normally graded ash | 829.5 | 1 | 4.5 | 9787 | 10841 | X | X | — | X | — |
| LLIII-08-86 | Beige lapilli | 878 | 1 | 2.2 | 10170 | 11000 | X | X | — | X | — |
| LLIII-08-90 | Gray normally graded coarse ash | 879 | 5 | 3.6 | 10175 | 11005 | X | X | — | X | — |
| LLIII-09-01 | Gray medium-coarse ash | 886 | 2 | 3.4 | 10187 | 11009 | X | X | — | X | — |
| LLIII-09-03 | Light gray lapilli layer | 888 | 2 | 0.7 | 10195 | 11010 | X | X | X | X | X |
| LLIII-09-15 | Fine gray ash | 900 | 2 | 3.1 | 10279 | 11038 | X | X | — | X | — |
| LLIII-09-22 | Reversely graded coarse ash to lapillia | 907 | 2.5 | 0.0 | 10326 | 11056 | X | X | — | X | — |
| LLIII-09-23 | | | | 1.6 | | | X | X | | X | — |
| LLIII-09-44 | Gray normally graded coarse-fine ash | 929 | 1.5 | 3.4 | 10494 | 11101 | X | X | — | X | — |
| LLIII-09-60 | Gray medium ash | 945.5 | 3.5 | 3.6 | 10626 | 11132 | X | — | — | X | — |
| LLIII-09-62 | | | | 0.6 | | | X | X | | — | — |
| LLIII-09-74 | Light gray fine ash | 960 | <1 | 4.8 | 10692 | 11148 | X | X | — | X | — |
| LLIII-09-98 | Coarse ash with some lapilli | 984 | 1 | 1.3 | 10786 | 11226 | X | X | X | X | — |

*Note.* SEM = scanning electron microscopy; LA-ICP-MS = laser ablation inductively coupled plasma mass spectrometry; EPMA = electron probe microanalysis.
[a]Insufficient grains to characterize.

Grain size data were gathered for each tephra deposit in each core. Bulk samples were oven-dried at 80 °C, sieved from −5 φ to 3 φ (32 mm to 125 μm) at one φ intervals and weighed. The 3 φ fraction was then recombined with the finer (<125 μm) material and analyzed by laser diffraction with a Malvern Mastersizer 3000 at the University of Bristol; five runs were performed per sample. The sieve (in wt%) and Mastersizer (in vol%) data were combined to reconcile the overlapping grain size, assuming a constant density across all grain sizes (Coltelli et al., 1998).

Each sample was prepared for backscatter electron (BSE) scanning electron microscopy (SEM). In most cases 1, 2, and 3 φ grain size fractions were prepared, although where insufficient 2 or 3 φ particles were present, smaller grainsizes were used. Particles were mounted in epoxy in an aluminium ring and polished to expose particle interiors. Polished mounts were then carbon coated before imaging with a Hitachi S-3500N SEM at the University of Bristol. For each grain size fraction a ~25-image mosaic was obtained and then combined using FIJI grid stitching software (Schindelin et al., 2012) to generate a high resolution image. Each image had a 1,024 × 769 pixel resolution and was taken at a working distance of ~20 mm and an accelerating voltage of 15 kV or 20 kV. Overall, between 150 and 1,200 grains were imaged per sample, depending on the grain sizes and the number of particles available.

Componentry analysis was performed to quantify the different grain components that comprise each tephra deposit. Each grain examined was classified into one of six categories (Figure 2): (1) lithic (microcrystalline), (2) crystal (proportion of mafic and felsic recorded), (3) crystal with adhered matrix (mafic and felsic recorded), (4) glass shard (presence of microlites recorded), (5) vesicular fragment, and (6) vesicular fragment with microlites (Figure 2). Lithics were identified by their blocky external 2-D morphology and heterogeneous appearance. The heterogeneity is provided by high crystallinity and near-absence of large (greater than several microns) patches of glass (Figure 2a).
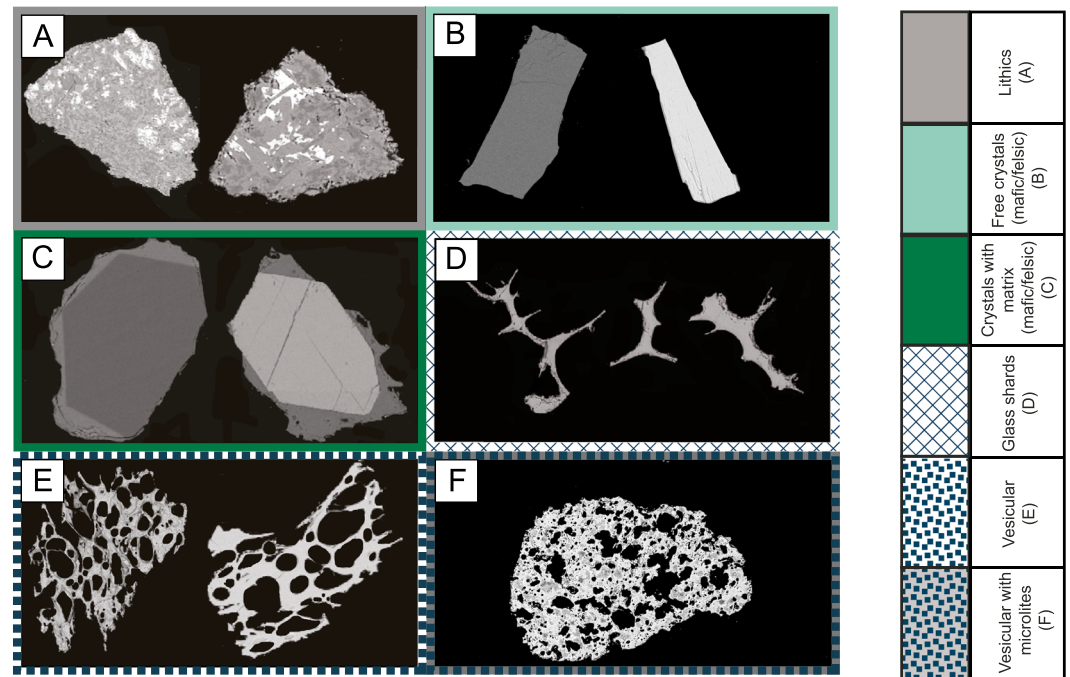
**Figure 2.** Scanning electron microscopy-backscatter electron images of different components counted from scanning electron microscopy imaging. (a) Microcrystalline lithic fragments, (b) mafic and felsic crystals (with no matrix attached) (c) mafic and felsic *free* crystals with matrix attached, (d) glass shard fragments, (e) microlite-free vesicular grains, and (f) microlite-containing vesicular grains. All components in the 3 $\varphi$ grain size fraction.

Ash grains comprising a single crystal (or crystal fragment) were classified into *mafic* and *felsic* based on their greyscale in BSE images, where Fe-Mg silicates such as pyroxenes have a larger mean atomic number and thus appear brighter than high-Si phases such as quartz and feldspar. In addition, mafic phases often show cleavage planes. In general, all crystals are equant with a semiquadrilateral 2-D morphology and are compositionally homogenous (Figure 2b). Specific identification of different mafic and felsic phases was not attempted from the BSE-SEM images, and so the proportions of different crystal types are not included.

Often, both felsic and mafic crystals retain some attached matrix of vesicular glass (presence of microlites recorded) or occasionally vesicle-free glass and rarely lithic fragments and are therefore counted as separate component. Grains were classified as *crystal with an adhered matrix* when the matrix component was <90% of the whole grain. Where the crystal occupied <10%, the particle was classified as whatever component comprised the remaining 90% (usually vesicular glass; Figure 2c).

Glass shards were identified and characterized based on greyscale and morphology. Glass has a greyscale similar to quartz and feldspar but typically has a more concave appearance than crystals (Figure 2d). Vesicular grains were differentiated from glass shards as glassy particles that contained at least one entire, unbroken vesicle (Figure 2e). The presence or absence of feldspar microlites (<20 micron crystals) in the glass was also documented. Feldspar microlites have only slightly lower mean atomic number than the surrounding glass and so required large image contrast to be identified (Figure 2f). The size, spacing, abundance, and composition of the microlites indicate crystallization within the magmatic system rather than secondary rehydration.

To determine the component proportions, each SEM mosaic was divided into a 4 × 4 grid. The components in each grid square were then recorded by point counting. The proportions of components were determined for samples from both cores, but ABII was chosen for a more comprehensive analysis because it represents a longer time period and contains the most tephra layers (Table 1). Componentry analysis was performed for (a) every major tephra sample (>~1-cm thick; equating to 18 different layers) in the ABII core for every 3 $\varphi$ fraction (and usually 1 and 2 $\varphi$), (b) the thickest samples in the LLIII core, and (c) LLIII layers that appeared to display similar textural features to specific ABII layers.

Major element geochemical data were collected by electron probe microanalysis using a JEOL JXA8530F Hyperprobe at the University of Bristol. Major elements were analyzed using a 2 nA beam current with a 10-μm spot size at a voltage of 15 kV. Count times were varied by element to optimize analysis time and count number while minimizing beam damage. Ca, Si, Al, Na, and K were analyzed first for 10 s, Ti for 80 s, Mg, F, Cl, and Fe for 60 s, and Mn for 30 s. In some cases MnO was not recorded due to a hardware problem; MnO is content is typically <0.2 wt% and therefore is not expected to have a significant effect on the overall results. The KN18 secondary standard was analyzed between each sample and was closely monitored throughout; no drift or deviation was observed during analysis. Only analyses with totals over 94% were retained, although the majority are over 97%. The lower totals are ascribed to secondary hydration from the lacustrine preservation environment. Where microlites were present in the glass, only microlite-free patches of glass large enough for a 10-micron spot size were analyzed. All plotted data are normalized to an anhydrous basis. If possible, at least 20 individual pieces of glass were analyzed per sample.

Laser Ablation Inductively Coupled Plasma Mass Spectrometry (LA-ICP-MS) at Trinity College, Dublin. The analysis was undertaken using a Thermo Scientific iCAPQ ICP-MS coupled to a Photon Machines analyte 193-nm eximer laser ablation system with a Helix two volume cell via an ARIS sample introduction capillary and an in-house signal smoothing device (poshDOG). The spot size was 30 microns and the repetition rate 10 Hz with a count time of 35 s (or 350 pulses). The calibration was performed using the NIST612 standard, and the internal standard was $^{29}$Si. The calibration was verified using the MPI-DING secondary glass standards ATHO-G and StHs6/80-G from the Max Planck Institute (Jochum et al., 2016). Accuracies are typically better than 10% for most elements, and reproducibility is better that 5 RSD% for all trace elements. We attempted to analyze 20 points per sample, although this varied slightly depending on the availability of large areas of glass.

Radiocarbon dates published by Gibert et al. (1999) for Lake Langano and Gibert et al. (2002) for Lake Abijata (8 in LLIII and 14 in ABII) were obtained from carbonates and organic material removed from lake sediment. We recalibrated the published ages using the most recent IntCal13 calibration curve as part of Oxcal version 4.3; all ages presented in this paper represent these recalibrated values (Figure 3; Bronk Ramsey, 2008; Bronk Ramsey & Lee, 2013; Reimer et al., 2013). To place more detailed constraints on the tephra ages, we further revised this existing chronology using Bayesian deposition modeling available through Oxcal (Bronk Ramsey, 2008; Reimer et al., 2013). Tephras were modeled using the *P sequence* function, including an outlier model (Bronk Ramsey, 2009). The Oxcal code can be found in the supporting information (text S1).

## 3. Results

### 3.1. Core Descriptions

The tephra in the two cores, ABII and LLIII, were easily distinguishable from lake sediments by color and grain size. Tephra is typically lighter in color, often beige to white, while lake sediments are darker gray and have a fine, homogenous grain size. Many of the tephras show grading (both normal and reverse; supporting information Figure S1) and contain little or no diatomite-rich lake sediment, suggesting that most layers represent a distinct eruption rather than remobilization events happening over a prolonged period of time. The top sections of both cores are missing, such that the time period accessible is 1.7 to ~12.5 cal. ka BP.

ABII has an 8.5-m long sediment record, which $^{14}$C dates indicate spans 1.7 to ~12.5 cal. ka (Chalié & Gasse, 2002; Gibert et al., 1999) and contains 25 distinct tephras (Figure 3a) with an average median grain size (Md) of 3.2 $\varphi$ (Table 1). The average tephra thickness is 3.64 cm, with the thinnest tephras <1 cm and the thickest 11 cm (Figure 3a). There are four tephra layers with thicknesses ≥5 cm. The thickest of these is ABII-04-62:73 (one layer subsampled three times), which is an 11-cm thick normally graded deposit with pumice lapilli at the base, fining upward to ash. The second thickest—ABII-10-73:75 (one layer, subsampled three times)—is 5-cm thick and shows normal grading with lapilli-sized pumice becoming coarser toward the base. The lower two of the three subsamples of this tephra have Md = 0.13 $\varphi$ and 0.14 $\varphi$ (one of the coarsest of all layers sampled from the core), whereas Md = 3.3 $\varphi$ in the uppermost subsample (Figure 3a).

LLIII has a 7.62-m long record which spans from 5.6 to 11.1 cal. ka BP (Gibert et al., 2002) and contains 21 tephra layers (Figure 3b) with an average median grain size of 2.5 $\varphi$ (Table 1). The average tephra thickness is 2.3 cm, with the thinnest tephras <1 cm and the thickest 6.5 cm. The thickest of these, LLIII-04-18, contains fine sediment with Md = 4.5 $\varphi$. The layer is described in the drilling log as a mixture of *mud and pyroclastics*
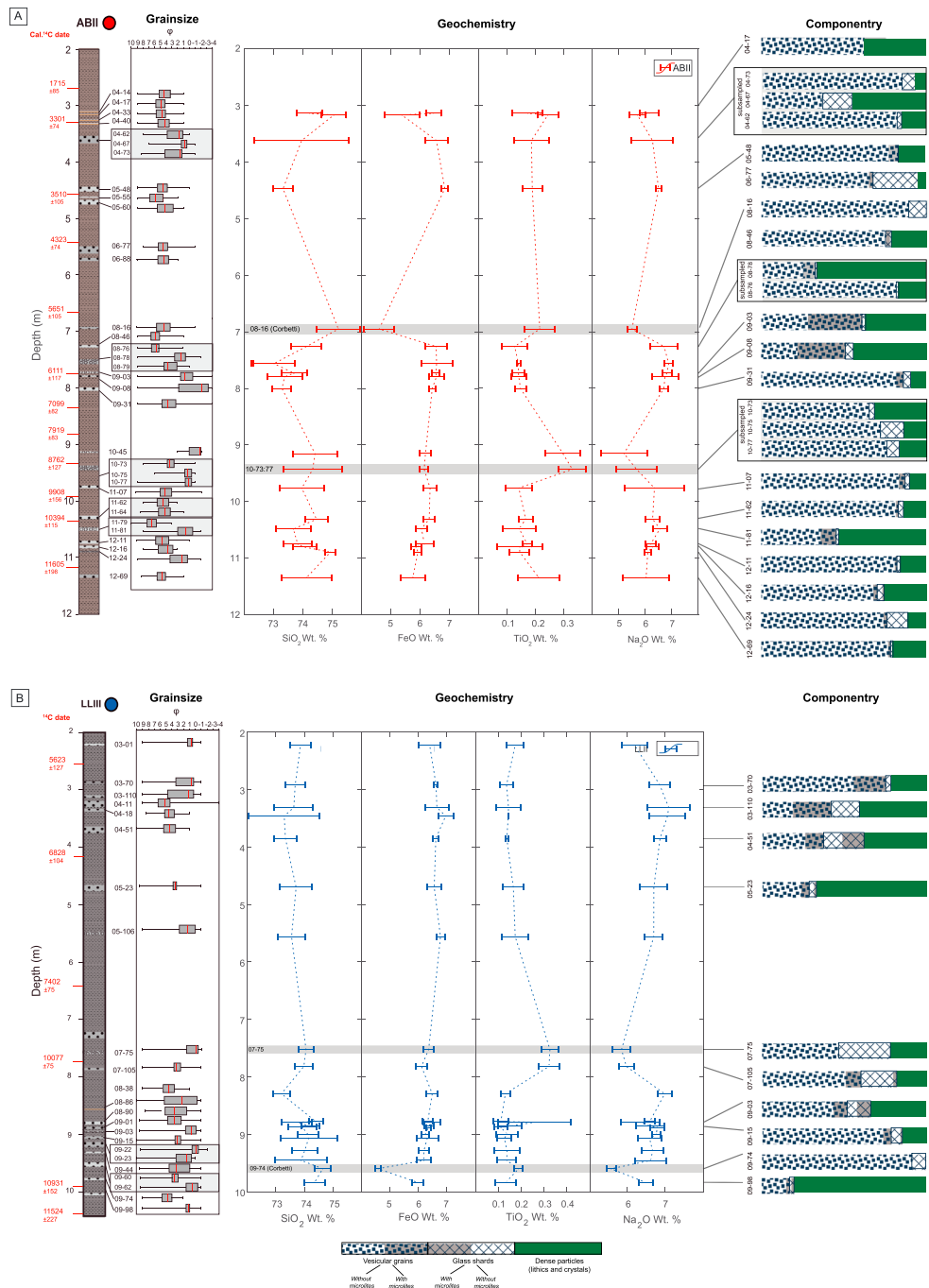
**Figure 3.** (a) Core log of core ABII. Calibrated $^{14}$C dates shown in red. Box and whisker plots of grain size data are shown for each sample and subsample. Red line indicates the median, the gray box indicates upper and lower quartile, and the whisker indicates grain size range. Geochemistry for analyzed tephras layers within each core is plotted with depth. Dashed lines are straight lines drawn between data points for legibility. Error bars represent one standard deviation to represent natural variation in the sample. The analytical error for each is calculated in the supporting information (Table S4) but in every case is lower than one standard deviation. Componentry is displayed for all tephras for which there were sufficient grains in the 3 $\varphi$ grain size fraction. Each bar represents 100%, with the colored and patterned sections indicating the proportion of different components. Green portion contains *dense* fragments described as crystals and lithics. Blue hatched pattern indicates glass shards, with the portion of microlite-containing glass shards in gray. Blue dots represent the vesicular portion, with microlite-containing vesicular grains shown in gray. Corbetti-sourced layer ABII-08-16 and glass shard layer ABII-10-73:77 are shown in gray. (b) Core log of core LLIII-legend as in (a). Componentry performed on all samples that could reasonably correlate with ABII based on an assessment of geochemistry, age and qualitative componentry. Corbetti-sourced layer LLIII-09-74 and glass shard layer LLIII-07-75 shown in gray.

(Gibert et al., 2002), contains a large amount of lake sediment amongst the ash, and does not display any grading or sorting. We infer that this layer to be the consequence of reworking, representing part of a turbidite deposit. These features are infrequently observed elsewhere in the core; the next three thickest layers (LLIII-04-51, LLIII-05-23, and LLIII-08-90) contain little lake sediment and preserve distinct boundaries with the nonvolcanic sediment above and below.

While we believe that LLIII-04-18 is the only turbidite deposit sampled, it is important to consider other forms of secondary reworking that may have affected additional tephra layers. In other settings, both secondary deposition via the fluvial system and redistribution by lake currents can generate greater than centimeter thick tephra deposits that can be misinterpreted as primary, especially where deposition occurs over the lake's watershed (Bertrand et al., 2014; Thompson et al., 1986). However, deposits cored from such settings are typically described as poorly sorted and contain pumices intermixed with finer ash and lake sediment. Deposits in Lakes Abijata and Langano often show clear grading, typically normal, which is not consistent with observations of fluvial deposits. In addition, the annual input to the modern Lakes Langano and Abijata is several orders of magnitude less than the input to lakes in other environments where fluvially thickened tephra layers are observed (i.e., Lake Puyehue in Chile), making it unlikely that large volumes of tephra will be deposited into the lake from the fluvial system (Ayenew, 2002; Bertrand et al., 2014; Zinabu et al., 2002). The depth of the lake must also be considered in the context of its effect on particle settling: both lakes have been subject to depth changes, with lake highstand periods sufficient to allow the two lakes to be connected the early Holocene. While it is not possible to accurately constrain the influence of lake depth on the deposits, we note that the tephra layers do not show any systematic differences between the early Holocene (lake level highstand) and late Holocene. In some cases, normal and reverse grading is apparent in consecutive deposits indicating that temporally close deposits were not the product of the same secondary processes. As all tephra layers show slightly different features regardless of position in the core, we infer that the deposits are most likely primary. As such, we interpret these thicknesses to represent of the true thickness of the primary deposit.

### 3.2. Major Element Composition

Results of electron probe microanalysis are presented in Figures 4 and 5, and all data and secondary standards are reported in the supporting information (Tables S1 and S4). All analyzed glasses are peralkaline in composition with 72–76 wt% $SiO_2$, with an average of 74.1 wt% and a relative standard deviation of 0.8.

In ABII, 17 out of 25 layers were analyzed for major elements. Of the eight layers not analyzed, most were in the top 2 m of the core, where they did not overlap temporally with LLIII. Of the 17 analyzed, major element concentrations were largely invariant and displayed little or no changes in eruptive composition throughout the Holocene, (e.g., $SiO_2$ = 74.0 wt% ± 0.99% ($1\sigma$)). This lack of geochemical variance was observed across all oxides and tephra samples, with the exception of three layers (Figure 3a). The youngest of these exceptions, ABII-08-16, is chemically evolved with an average $SiO_2$ = 75.2 wt%, compared to a core average of 74.0 wt%. More noticeably, the layer has an average FeO = 4.6 wt%, which is 26% lower than the core average (Figure 3a). The other two geochemically distinct layers are ABII-10-45 and ABII-10-73:77, which both contain an average of 0.3 wt% $TiO_2$ (70% above the core mean) and $Na_2O$ = 5.5 wt% (11% below the core mean; Figures 3a and 5).

In LLIII, 20 layers were analyzed for major element concentrations. Like the ABII core, the tephra glasses have homogenous major element concentrations with an average $SiO_2$ = 73.8 wt% ± 0.5% ($1\sigma$). There is little variation in any major element oxides, with the exception of three layers (Figure 3b). The youngest of these are layers LLIII-07-75 and LLIII-07-105, which occur consecutively in the core. These layers have a $TiO_2$ value of 0.3 wt% (100% above the core mean) and an $NaO_2$ value of 5.9 wt% (11% below the core mean) (Figures 3b and 5). The final layer with unique chemical characteristics is LLII-09-74, which has a higher than average $SiO_2$ value of 74.6 wt% and lower than average FeO of 4.6 wt% (compared to a core average of 6.3 wt%; Figures 3b and 4).

### 3.3. Componentry

Componentry analysis was undertaken on 23 samples in ABII comprising 18 different tephra deposits. The proportion of dense (crystals and lithic fragments) to glassy (glass shards and vesicular grain) varies with depth in the core and does not appear to be systematic (Figure 3). The only sample without dense
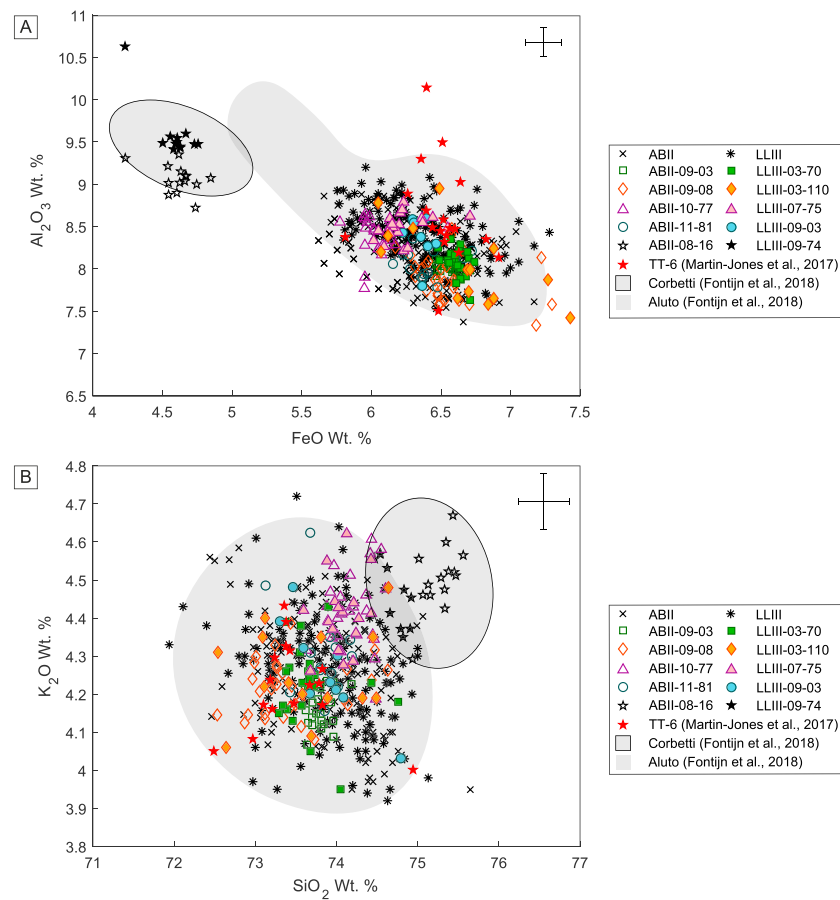
**Figure 4.** Bivariate plots of glass major element geochemistry. Certain layers are plotted in color to highlight the difficulties with correlating using major element geochemistry with such a large number of units that occupy a small geochemical range. Reference glass geochemical data for Aluto and Corbetti from Fontijn et al. (2018) shown in gray field. TT-6 a tephra layer in sediment core from lake Tilo (~100 km SW Aluto) and thought to be sourced from Aluto (after Martin-Jones et al., 2017) is plotted as red stars. Layers thought to be from an eruption of Corbetti volcano are plotted as black 5-point stars. An average standard deviation for the plotted layers is shown in the top right.
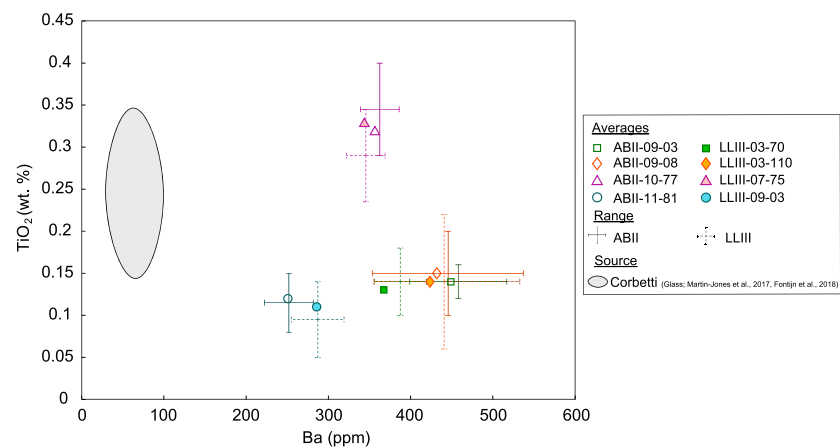


**Figure 5.** Plot showing Ba (ppm) and $TiO_2$ (wt%). Ranges are shown for both as it was not always possible to analyze the same grain for the majors (i.e., TiO2) and trace elements (i.e., Ba). Markers display the average value for each. For comparison, the $TiO_2$/Ba window for Corbetti is plotted (gray with black line) from Fontijn et al. (2018; $TiO_2$ data) and Martin-Jones et al. (2017; Ba data).
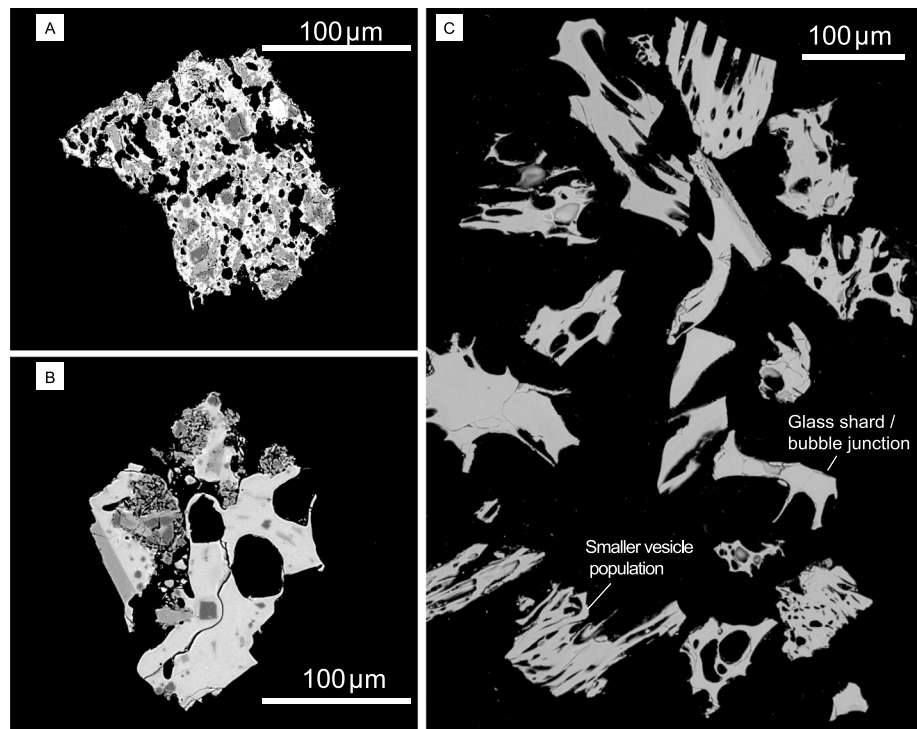
**Figure 6.** Scanning electron microscopy-backscatter electron images showing the variations in microlite and glass shard texture. (a) A vesicular grain from ABII-09-03 containing densely packed microlites, which have caused the vesicles to form in irregular vesicle networks. (b) A microlite-bearing vesicular grain with fewer microlites from ABII-11-07. In this case, the microlites have had almost no effect on the formation of bubbles, which are comparatively spherical. (c) Image of LLIII-07-75. Displays the characteristic *glass shards* which have formed from the fragmentation of a larger bubble population. A smaller bubble population is still preserved in the more vesicular grains.

particles is ABII-08-16 (Figure 3a). The crystal components comprise a range of phases, with typical felsic components including quartz and alkali feldspar (sanidine), while the mafics include alkali pyroxene (aegirine), aenigmatite, and Fe-Ti oxides.

Within the glassy portion, the presence and abundance of glass shards is also variable. Particularly notable for their high proportions (>10%) of glass shards are ABII-04-62:67 (one layer subsampled three times), ABII-06-77, ABII-08-16, and ABII-10-73:77 (one layer subsampled three times; Figure 3a). Two of these layers (ABII-06-77 and ABII-10-73:77) have a distinctive shard morphology, with highly concave glass shard fragments that represent the remnants of walls of relatively large (~50–100 μm) bubbles. These glass shards are accompanied by other grains that contain a smaller vesicle population (Figure 6c).

The presence of microlites in the glass also varies, with layers ABII-09-03, ABII-09-08, ABII-11-07, and ABII-11-79:81 (one layer subsampled twice) showing particularly high proportions of microlite-bearing glassy particles. Of these, layers ABII-09-03 and ABII-09-08 contain densely packed microlites, which affected vesicle growth, producing irregularly shaped vesicle networks in the grains (Figure 6a). In contrast, microlites are more sparse in the vesicle-containing grains in the earlier layers (ABII-11-07 and ABII-11-79:81), and as a consequence most of the vesicles are near-circular in cross section (Figure 6b).

The proportions of components were quantified in only 10 layers of the LLIII core. These layers are not representative of the core, and some were chosen specifically because of anomalous componentry (e.g., high microlite content) based on qualitative assessment of BSE images. The only sample that does not contain any dense fragments is LLIII-09-74. The proportions of dense versus glassy grains is variable, with four layers containing high proportions of glass shards: LLIII-03-110, LLIII-04-51, LLIII-07-75, and LLII-07-105 (Figure 4b). Of these, LLIII-07-75 contains shards with highly concave, bubble-wall shards (e.g., Figure 6c). Layers LLIII-03-70, LLIII-03-110, LLIII-04-51, LLIII-07-105, LLIII-09-03, and LLIII-09-15 (Figure 4b) are notable for having

grains with microlites. Of these, two (LLIII-03-70 and LLIII-03-110) contain densely packed microlites which affected the vesicle structure (Figure 6a).

### 3.4. Trace Element Composition

Because the major element chemistry was not sufficiently distinctive to uniquely fingerprint different tephra layers, we performed trace element analyses on selected samples with distinct textures: (1) high-microlite content (ABII-09-03, ABII-09-08, LLIII-03-70, and LLIII-03-110; Figure 6a), (2) lower microlite content (ABII-11-79:81 and LLIII-09-03; Figure 6b), and (3) concave glass shards (ABII-10-73:77 and LLIII-07-75; Figure 6c; supporting information Table S3). While many trace elements varied with respect to particle textures, Ba shows the clearest variation (Figure 5). The high-microlite content layers have glass with relatively high Ba concentrations (348–532 ppm) and the low-microlite layers contain lower Ba (222–319 ppm); these variations are consistent with incompatible behavior of Ba. The glass shard layers contain Ba between 326 and 386 ppm; these layers are easily identified by their high $TiO_2$ values (Figure 5). As it was not always possible to analyze the same grain for major and trace element compositions, the range of values for each unit is shown in Figure 5, as well as the average of all grains analyzed in each layer. Our values are within the range of published whole-rock data for Aluto (Hutchison, Pyle, et al., 2016).

### 3.5. Corbetti Versus Aluto Tephra Source

The location of the coring sites means that we expect the tephras to be predominantly from Aluto and almost all have a peralkaline rhyolitic composition consistent with this source (cf. Fontijn et al., 2018; Figure 4). However, ABII-08-16 and LLII-09-74 have a clearly different glass composition and componentry (Figures 3; 4). Their lower FeO content compared to all other samples, and relatively high $SiO_2$, $K_2O$, and $Al_2O_3$, match the composition of products of Corbetti volcano, the silicic center approximately 80 km south of Aluto, 50 km south of ABII, and 60-km south of LLIII (Fontijn et al., 2018; Martin-Jones et al., 2017). ABII-08-16 and LLLII-09-18 are also the only two samples that contain no dense material, including no crystals (Figure 3); the lack of crystals is consistent with most eruptions of Corbetti (Fontijn et al., 2018; Mohr, 1966; Schmincke, 1974). Modeled Oxcal ages indicate that ABII-08-16 was deposited between 5,410 and 5,980 cal. year BP and LLIII-09-74 between 10,690 to 11,140 cal. year BP, which agrees with known periods of explosive activity at Corbetti, as constrained by tephra deposits found in lake sediment cores south west of Corbetti (Fontijn et al., 2018; Lamb et al., 2002; Martin-Jones et al., 2017). We interpret the two tephra layers to be the product of two different eruptions of Corbetti. Given that they are the only entirely aphyric samples observed in the cores, and their distinct geochemistry, we are confident that these are the only Corbetti-sourced layers in our sample suite and exclude them from our subsequent study of Aluto's eruptive history.

## 4. Discussion

Our study of tephra from two lake cores provides detailed constraints on the Holocene eruptive history of Aluto. We believe Aluto to be one of the most frequently active volcanoes in the region (Fontijn et al., 2018; Hutchison, Fusillo, et al., 2016; Hutchison, Pyle, et al., 2016), and so developing understanding of eruption size and frequency is key to improving hazard assessment. The two cores, LLIII and ABII, are positioned 12 km south and 25 km south west of the volcano, respectively. When drilled, ABII spanned the longest time interval, representing sediment deposition from ~0.2 to 13.4 cal. ka BP, while LLIII spanned ~5.1 to 11.5 cal. ka BP. However, the top sections of both cores are now missing, meaning the time periods available for this study are ~1.7 to 11.6 cal. ka BP and ~5.6 to 11.5 cal. ka BP, respectively, and should overlap for the period of ~5.6 to 13.4 cal. ka BP.

The tephras in ABII are on average thicker than those in LLIII despite being further from Aluto. Wind reanalysis data from 2015 and 2016 indicate a west-south-west prevailing wind direction (as per the methods of Kalnay et al., 1996), which is consistent with thicker ash fall deposits in ABII. Coupled with the fact that the lake cores are more likely to preserve fine ash than terrestrial sequences, they provide the opportunity to generate a well-constrained record of the volcano's Holocene activity. This record can be used in conjunction with (now) terrestrial distal deposits to determine eruption styles and frequency of activity at the volcano. Here we first discuss methods of correlating the lake core tephras, before evaluating the implications of the tephra record for eruption dynamics and Aluto's Holocene eruption history.

### 4.1. Correlating the Cores

The majority of tephras in both cores have similar major element compositions. The only obvious exceptions to this are the samples interpreted as Corbetti-sourced samples, which are discounted from further discussion. Beyond these, the only layers to display any geochemical distinction are LLIII-07-75, LLII-07-105 in LLIII, and ABII-10-45 and ABII-10-73:77 in ABII. Unlike the Corbetti layers, these have FeO and $SiO_2$ values that are indistinguishable from other samples but show variations in other elements, particularly $TiO_2$.

All four of these layers have $TiO_2$ values of ~0.33 wt% (approximately 80–100% higher than the core mean; Figures 3 and 6). This unusually high $TiO_2$ is complemented by lower than average $Na_2O$ (~11% lower than the core mean) in the same layers (Figure 3). The layers are preserved between ^{14}C dated material of comparable ages: ABII-10-45 lies between 7,919 ± 83 and 8,762 ± 127; ABII-10-73:77 lies between 8,762 ± 127 and 9,908 ± 156 cal. year BP and LLIII-07-75 and LLIII-07-105 between 7,402 ± 75 and 10,077 ± 75 cal. year BP. LLIII-07-105 is a fine, thin ash layer which, when examined on the SEM contained very little pyroclastic material larger than 100 $\mu$m. Similarly, ABII-10-45 is a thin (<1 cm) layer, containing mostly subrounded lapilli and little other volcanic material. As such, we infer that the two thicker layers, which are 4.5- and 5-cm thick (ABII-10-73:77 and LLIII-07-75, respectively), represent the same eruption. The thinner layers may be smaller events that occurred before and after the larger eruption. It is also possible that as ABII-10-45 appears after ABII-10-73:77, it is a reworked and redistributed component of the larger layer below. However, while the two layers show the same glass chemistry, ABII-10-45 does not show the same high component of glass shards as ABII-10-73:77 and we therefore interpret it as another, much smaller eruption with a similar composition.

While the identification of three high-$TiO_2$, low-$Na_2O$ tephras was possible with major elements alone, the chemical similarity of the glass in most ash layers required other methods of correlation. Although the same grain size fraction is compared throughout, the proportion of dense versus glassy fragments was not a useful correlative tool, likely because of the factors relating to eruption size, direction and the settling of different components discussed in section 1.2. However, variations in relative proportions of other grain components (as detailed in methods and Figure 2) were useful for some correlations.

Particularly useful for correlation was the presence and abundance of microlites within glassy grains, and the presence and abundance of glass shard fragments. For example, the high $TiO_2$ layer in ABII (ABII-10-73:77) and an approximately isochronous high $TiO_2$ layer in the LLIII core (LLIII-07-75) contain a greater proportion of large (~125–250 $\mu$m) glass shards than surrounding tephras (Figure 3). The shards themselves also have a highly convex morphology not observed elsewhere in the LLIII core (Figure 6). This morphology indicates that they are remnants of bubble junctions rather than equant, blocky glass fragments (Figure 6). The similarity in form and age suggest that these layers are likely the product of the same eruption (termed Aluto Glass Shard Layer—AGSL1—in this study; Figure 7). Coupled with the $TiO_2$ signature, AGSL1 is a useful, identifiable marker unit. Indeed, we had identified this glass shard layer as the product of the same eruption before geochemical data were obtained to support the correlation. Another tephra with a high proportion of similarly concave glass shards was observed in the top half of the ABII core. However, this layer, ABII-06-77, (Oxcal age: 5323–5840 cal. year BP) is likely too young to also be recorded in the LLIII core and therefore cannot be correlated.

The presence and textures of microlite-containing glass particles allowed correlation amongst more geochemically similar tephra layers. Microlites were documented in 12 of 19 layers in ABII, although the proportions of microlite-containing to microlite-free glass varied considerably within these layers. In the ABII core, the four layers that contain the highest proportion of microlite-containing glass relative to microlite-free glass are ABII-09-03, ABII-09-08, ABII-11-07, and ABII-11-79:81 (Figure 3a). The first two appear consecutively in the core. Layer ABII-09-03 was deposited between ^{14}C dated material with recalibrated ages of 5651 and 6111 cal. years BP, and ABII-09-08 between material recalibrated to 6111 and 7099 cal. yr BP (Figure 7). Here microlite-rich grains constitute up to 33% of the total observed grains. SEM-BSE images show that the microlites are closely spaced and have produced irregularly shaped vesicle networks (Figure 7). There are several microlite-rich layers in LIII that were deposited during a similar time interval: three were deposited between 5623 and 6828 cal. yr BP and one between 6828 and 7402 cal. yr BP (Figure 3b). Of these four layers, the first two (LLIII-03-70 and LLIII-03-110) and the second two (LLIII-04-51 and LLIII-05-23) are consecutive, meaning there are two pairs of microlite-rich tephras preserved within a time period comparable to the ABII microlite-rich tephras.
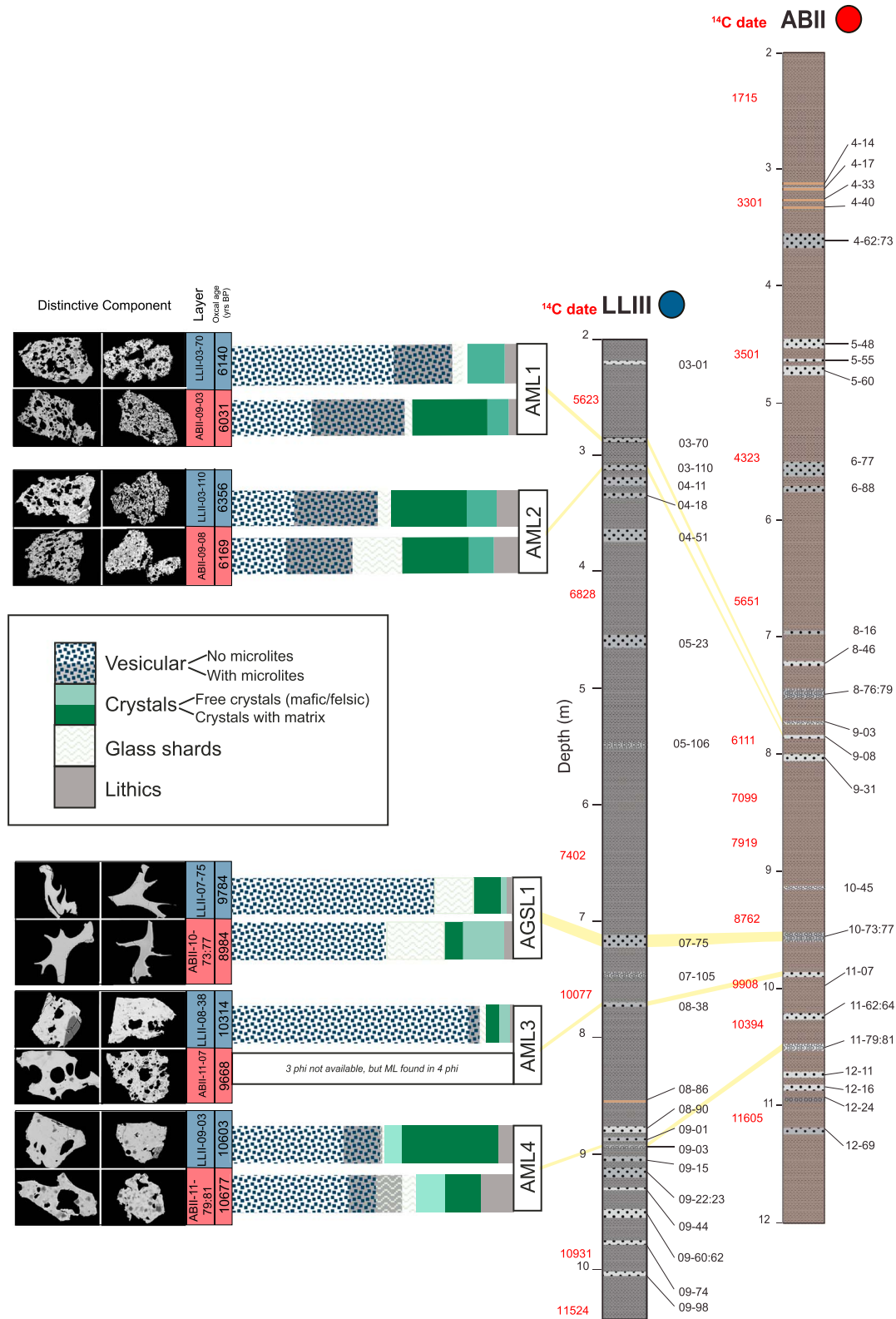
**Figure 7.** A summary of correlations made using componentry analysis. All componentry data shown is the for 2 φ grain size fraction. AML1 and AML2 are correlated based on the high proportion of microlite bearing grains, in which the microlites are closely spaced and affect vesicle textures. AGSL1 contains a high proportion of glass shard fragments, while AML3 and AML4 contain microlite bearing glassy fragments with sparse microlites. The medians of the Oxcal-modeled tephra ages are shown.

**Table 2**
*Summary of Correlations Made Between Cores ABII and LLIII From Lakes Abijata and Langano*

| | | Reasons for correlations | | |
|---|---|---|---|---|
| ABII layer | LLIII layer | Major element geochemistry | Texture | Trace elements |
| ABII-09-03 | LLIII-03-70 | Nonunique major element concentrations | High proportion of dense microlites | For example, high barium concentration |
| ABII-09-08 | LLIII-03-110 | Nonunique major element concentrations | High proportion of dense microlites | For example, high barium concentration |
| ABII-10-73:77 | LLIII-07-75 | High $TiO_2$ | High proportion of glass shards | For example, high calcium concentration |
| ABII-11-07 | LLIII-08-38 | Nonunique major element concentrations | High proportions of sparse microlites | For example, low barium concentration |
| ABII-11-79:81 | LLIII-09-03 | Nonunique major element concentrations | High proportions of sparse microlites | For example, low barium concentration |

*Note.* The features which have allowed these five layers to be correlated are detailed, including the $TiO_2$ content of the glass, proportions of different ash components (quantified from scanning electron microscopy images) and the trace element glass composition- particularly Ba and Ca concentrations.

To determine which LLIII pair correlates with the ABII pair, the microlite and vesicle textures were examined in greater detail. In LLIII-04-51 and LLIII-05-23, the microlites typically occupy <~10% of the glass, the vesicles have simple, near-circular shapes in BSE images (Figure 6b), and the grains containing microlites constitute a small proportion (between 7% and 15%) of the total glassy grains. The other pair, LLIII-03-70 and LLIII-03-110, have abundant (25%–30%) grains containing densely packed microlites and irregularly shaped vesicle networks (Figure 6a; Figure 7). Consequently, we correlate these two tephras with the same eruptions that deposited ABII-09-03 and ABII-09-08; we call them tephras AML1 (Aluto Microlite Layer 1) and AML2, respectively (Figure 7). Texturally and temporally equivalent layers to LLIII-04-51 and LLIII-05-23 are not present in the ABII core, suggesting that the eruptive deposits either did not reach, or were not preserved, in the more distal Lake Abijata.

The other microlite-rich layers in ABII, ABII-11-07, and ABII-11-79:81, were correlated with LLIII in much the same way as AML1 and AML2. Recalibrated ^{14}C dates suggest ABII-11-07 was deposited between 9908 and 10394 cal. year BP and ABII-11-79:81 between 10394 and 10931 cal. year BP. There are nine tephras deposited in the LLIII core within a similar time period. Of these, only three contain comparable proportions of microlitic material (LLIII-08-38, LLIII-09-03, and LLIII-09-15), with LLIII-09-15 containing a far lower proportion of microlitic material than the other two (Figure 3b). Consequently, we correlate ABII-11-81 with LLIII-09-03 (eruption is termed AML3) and ABII-11-07 with LLIII-08-38 (eruption AML4) (Figure 7).

Trace element data for AML1, AML2, AML4, and AGSL1 support these correlations, with Ba found to be particularly effective in distinguishing between the correlated layers (Figure 5). It should be noted that other trace elements, particularly Zn and Ca (see supporting information Table S2), have similar trends, although Ba is the most pronounced. The glasses in layers comprising AGSL1 have very similar Ba concentrations clustered tightly at around 350 ppm. The two layers that comprise AML4 contain 50–100 ppm less Ba than the other layers and thus appear distinctive and correlatable. Experimental data indicate that Ba partitioning into feldspar decreases with decreasing Ca content and consequently, increasingly peralkalinity. (Henderson & Pierozynski, 2012). As a result, Ba may behave incompatibly in this setting, providing a useful element to assist with correlating by componentry. The glass compositions of tephras containing densely packed microlites (AML1 and AML2) are more variable, however, (consistent with varying crystallinity) and thus harder to constrain using trace element data. The layers comprising AML1 showed some differences in Ba concentration, with LLIII-03-70 ranging from 350 to 430 ppm, while ABII-09-03 ranged from 400 to 500 ppm. The layer immediately below it in the core (AML2) spans the range occupied by AML1, with Ba 350 to 500 ppm (Figure 5). For these layers we infer the crystallization of microlites is causing localized changes in the melt concentrations of trace elements. Consequently, it appears that componentry analysis is the most effective method for correlating layers with complex microlite textures.

In summary, we have been able to correlate a total of five tephra layers between the two cores (Figure 7 and Table 2). To achieve this, we used several techniques which, when used in isolation, do not allow for confident correlations. Major element values showed large overlap but componentry analysis proved useful. Layers correlated using componentry show either distinctive glass shards with a unique chemical composition or a considerably higher proportion of microlite bearing grains (~100% more in the ABII core) than other tephra layers in the core. This means that microlite-rich layers can be identified with relative ease using SEM analysis. Correlations of these layers are confirmed with trace element analysis (Figure 5) and are consistent with

timing and position in the core. Importantly, however, correlations are difficult to confirm using either geochemistry or textural data alone. Additionally, the many other tephra layers in the cores, while typically microlite-bearing, are not sufficiently distinct to allow definitive correlation.

Some tephra layers identified in lake sediment cores 40 km WSW of Corbetti have similar compositions to our Aluto tephras; specifically, Martin-Jones et al. (2017) identified indicate two nonCorbetti sourced tephras in a core of lake Tilo (~100 km south west of Aluto). One of these, TT-6, is ~1-cm thick and shows geochemical similarities to many of the Aluto core tephras (Figure 4). From its Oxcal modeled age of 2672–2159 cal. year BP we infer that TT-6 most likely corresponds to the thickest of the ABII tephras (ABII-04-62:73), which is 11-cm thick and has a modeled age of 3167–3612 cal. yr BP. However, this correlation is not confirmed with componentry or trace element data.

### 4.2. Calculating an Eruption Frequency

The lake sediment cores represent a continuous record of Holocene eruptive activity from Aluto volcano. Unlike terrestrial sections, which may be subject to remobilization, erosion, and pedogenesis, lake tephras can record relatively small events (e.g., Kuehn & Negrini, 2010; Moreno et al., 2015) and consequently preserved a good record of Aluto's Holocene eruptive history. To quantify this, we have analyzed the sequence of tephra ages obtained from Oxcal modeling.

The Oxcal model calibrates tephra ages starting with the $^{14}C$ dates provided from the two paleoclimate studies (Chalié & Gasse, 2002; Gibert et al., 1999, 2002). The model provides an upper and lower bound for each tephra layer, bu for simplicity, we use the median values. As the only dates available are the $^{14}C$ values from the paleoclimate studies, the modeled tephra ages depend on the accuracy of these dates.

The medians of each of the correlated layers are shown in Figure 8 and Table 1. AML1, AML2, and AML4 have comparable Oxcal ages, with the medians of the modeled dates falling within ~200 years of each other. The median ages of AGSL1 and AML3, in contrast, differ in the two cores by several hundred years (Figures 7 and 8): layers identified as AGSL1 are ~800 years apart, while the units comprising AML3 are ~650 years apart. There is, however, overlap between the upper and lower bounds of the Oxcal ages in both cases (Table 1) indicating that despite the bigger gaps in the median ages, the ages are still within error.

It is possible that the low overlap in age for the AML3 and AGSL1 layers is because of the corrections made to $^{14}C$ dates in the cores. Lake Langano has been subject to $CO_2$ degassing through a fault system outcropping under the lake (Gibert et al., 2002). While the authors corrected for this $CO_2$ emission based on modern levels of $CO_2$ degassing, it is possible that the $CO_2$ output from the fault has not been constant over time. Lakes Langano and Abijata were also joined during a humid period in the early Holocene (Benvenuti et al., 2002, 2013; Chalié & Gasse, 2002; Le Turdu et al., 1999). Consequently, any reservoir effects may have affected both cores to an unknown degree. While the authors of both chronologies have applied corrections to the measure ages, it may not have been possible to fully account for the effects which influenced the $^{14}C$ ages and, as a result, our tephra Oxcal ages.

Core ABII contains 24 Aluto-sourced tephras deposited over a time span of 8,990 years equating to, on average, one eruption every 375 years. LLIII contains 20 Aluto-sourced tephras over 5,439 years, indicating one eruption every 272 years. It should be noted that LLIII is closer and so likely to record more eruptions. To assess the temporal variability, we plot the survival function ($S_T$) for both cores (Figure 8):

$$S_T = \frac{N - i}{N},$$ (1)

where $N$ is the total number of repose intervals and $i$ the number of eruptions up to that point in time (e.g., Connor et al., 2003). As LLIII does not cover the same age range, the curve was modified based on the ages and locations of the $^{14}C$-dated material, so the LLIII curve begins at the same time as a similarly aged ABII point. This assumes that up to that point, the LLIII core would have contained the same number of tephra layers as the ABII core, should its record have extended back as far.

Layers in ABII occur at irregular time intervals. There are three periods where the gradient of the survival function is steeper (more eruptions per unit of time ~3.5, ~6, and ~11 ka) and two periods where it is flatter (fewer eruptions: at ~5 and ~8 ka) giving it a stepped appearance. LLIII shows similarly variable eruption recurrence
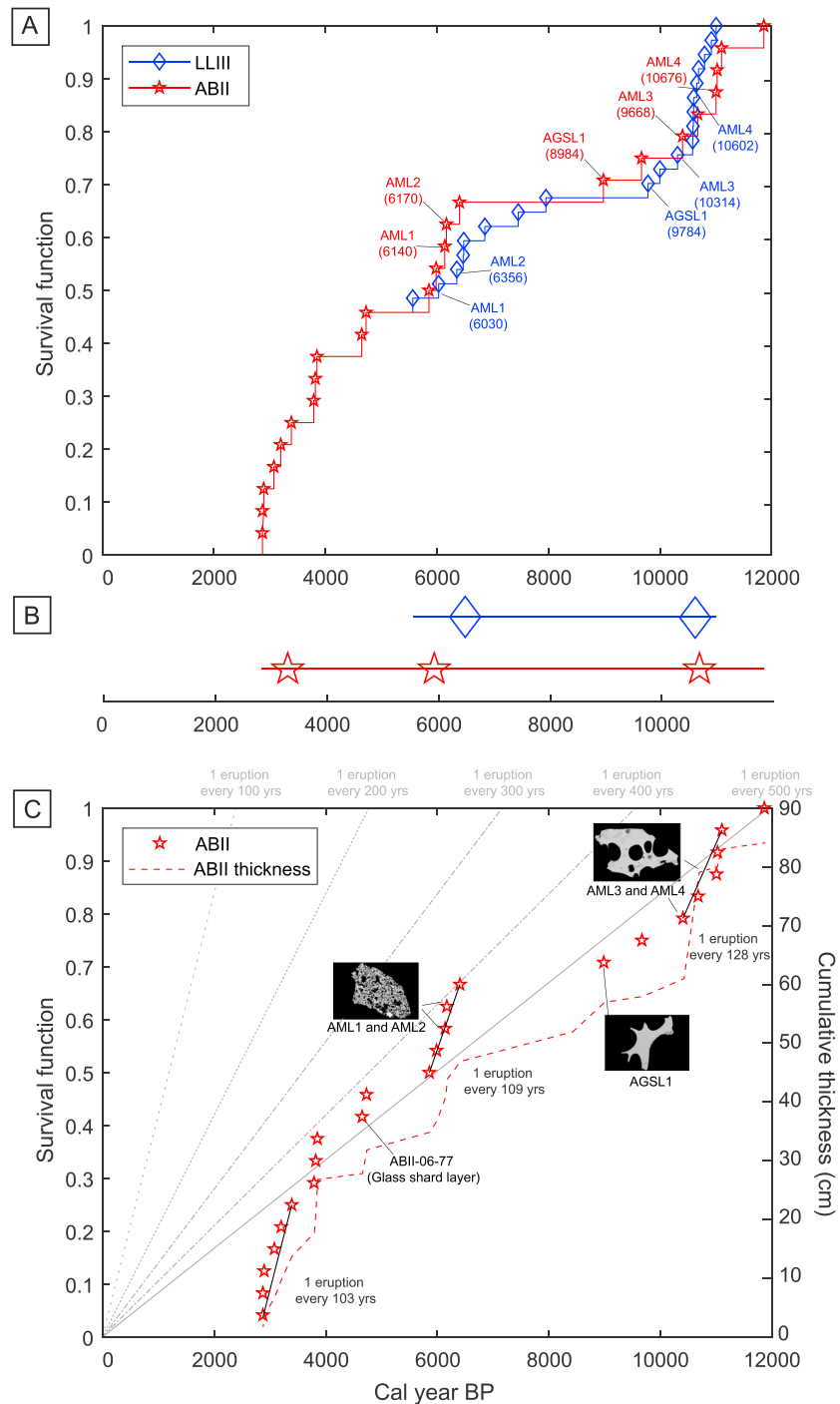
**Figure 8.** (a) Plot of survival function with time for core ABII (red) and core LLIII (blue). The correlated layers are labeled, with the ABII layers in red and the LLIII layers in blue. The medians of the Oxcal modeled ages are in brackets. (b) Centroids of the three main periods of increased activity are shown. This is defined as any cluster containing five or more tephras with an eruption frequency greater than one eruption every 150 years. (c) Plot highlighting the three clusters in ABII that correspond to periods of increased tephra deposition (red dashed line) and consequently, increased tephra thickness. Correlated layers with their unique textures are also shown. Note ABII-06-77, which is not correlated with a LLIII layer but has a high proportion of glass shards (as seen in AGSL1). Gray lines indicate the gradients of various eruption frequencies which can be compared to the gradients of the clusters as well as the period of repose.

intervals. The LLIII core is shorter, however, and contains only two periods of increased activity (i.e., the survival function has a high gradient; Figure 8a) and one lower-frequency period (at ~9 ka). The two periods of heightened eruptive activity in the overlapping portion of the two cores are slightly offset, with the flat portion of the survival function beginning and ending ~800 years earlier in LLIII than ABII. This offset is consistent with the offset observed in the modeled ages of the correlated tephra layers. The apparent offset between the two cores could be a consequence of the aforementioned $CO_2$ degassing into Lake Langano that may have affected $^{14}C$ dates. LLIII also records more eruptions than ABII, which is expected given its proximity to the volcano (Figure 8a). While this may have resulted in some underrecording in ABII, because the cores record similar eruptive patterns (i.e., periods of increased activity), we interpret the nonlinear eruption pattern to be real and not an artifact of tephra preservation.

The stepped-like appearance of the survival function for the two cores (Figure 8a) indicates that the volcano has seen pulses of increased activity alternating with periods characterized by longer repose intervals. To quantify the eruptive *pulses*, cluster analysis was undertaken using the *k*-means function in Matlab vR2017a. The function uses a Euclidean distance measure and the *k*-means ++ algorithm. The cluster algorithm was run for a varying number of clusters from two to 10.

The clustering analysis was run separately for the two cores. Although the algorithm yielded several clusters for each core, we focus on three clusters that represent heightened eruptive activity. In each case, these clusters include five or more consecutive eruptions with a maximum repose time of 150 years. The cluster centroids in both cores appear at approximately 3.5, 6, and 11 cal. ka BP (Figure 8b). While there are other eruptions in the periods between the clusters, they occur at lower frequencies. The three *active* periods represent eruptions every 103, 109, and 128 years (Figure 8c), whereas the two intervening *quiet* periods include activity every 519 and 1,700 years. High-frequency eruptive episodes deposited more tephra over a smaller time period, as illustrated by plots of cumulative thickness (Figure 8c). Episodic behaviors on varying timescales have been observed in other volcanic systems and are associated with the interactions between magma evolution, ascent, degassing, and crystallization (e.g., Fontijn et al., 2015; Sheldrake et al., 2016). As Aluto displays noncyclicity in the eruption recurrence, methods of forecasting that assume a mathematically constrainable periodicity (i.e., failure models such as a Weibull distribution; Ho, 1996) are not necessarily applicable (e.g., Connor et al., 2003).

### 4.3. Eruptive Activity

While the cores provide key information about eruption frequency, it is difficult to estimate eruption magnitude without more detailed spatial information. Critically, the characteristics of a deposit at a single location depend on both the eruption dynamics (e.g., intensity and duration) and the strength and direction of the wind at the time of dispersal. We can make some preliminary inferences about wind direction. It is well established that fall deposits thin and become finer-grained with distance from the volcanic vent when measured along the dispersion axis (e.g., Pyle, 1989). However, the tephras in the more distal ABII core are, on average, slightly thicker than those in the more proximal LLIII core. This pattern suggests that the wind typically directed the ash clouds more toward ABII than LLIII. While we cannot corroborate this robustly, this interpretation is consistent with modern conditions which indicate an east-northeasterly prevailing wind (Kalnay et al., 1996). There are methods to estimate eruption size when a deposit is well sampled and documented, although it is not reasonable to apply them to eruptions with data from only two locations (two lake cores), especially without total confidence in the wind direction.

However, we can make some estimates of eruption size based on the thickness of the deposits (e.g., Pyle, 1989). Both the magnitude of the eruption ($M = \log_{10}[\text{mass erupted in kg}] - 7$) and the thickness of the deposit depend on the eruption intensity (mass eruption rate) and eruption duration. To illustrate the possible eruption sizes that produced the Aluto tephras, we compare the thickness of the deposits with those of other well-studied eruptions at equivalent distances. For example, the average thickness of tephra in the ABII core 27 km from the volcano is 3.8 cm. This is comparable to the fall deposit produced by the 2015 $M \sim 4$, sub-Plinian eruption of Calbuco in Chile, with tephra <5-cm thick at ~30 km from the volcano (Castruccio et al., 2016).

The thickest deposit in the ABII core is 11-cm thick. This is comparable to the thickness of tephra deposited during the wind-still ~4 ka Plinian eruption of Rungwe in Tanzania; the deposit from this $M$ 5–5.3 eruption is

approximately 15-cm thick at ~30 km from the volcano (Fontijn et al., 2011) with 1- to 3-cm deposition 115 km from the source. At least one tephra layer with a comparable major element composition to Aluto was found in lake cores ~100 km south west of Aluto by Martin-Jones et al. (2017; Figure 4). In lake Tilo, this layer (TT-6), is ~1-cm thick. If it represents the same eruption as the 11-cm ABII layer, then Aluto had at least one Holocene eruption with a maximum size comparable to the Rungwe Pumice wind-still eruption. In reality, the Aluto eruption likely displayed some ash cloud directionality to the southwest (as discussed above), meaning that it was probably smaller.

The thinnest tephras deposited in the ABII core are <1 cm. The 2011 sub-Plinian to Vulcanian eruption of Kirishima in 2011 produced a highly directional ash plume depositing tephra of up to 1-cm thick about 30 km from source along the dispersal axis (Miyabuchi et al., 2013; Nakada et al., 2013). Therefore, based on comparisons to dispersion patterns from eruptions of other volcanoes, we suggest that eruptions of Aluto between ~2 and 12 ka produced deposits comparable to those of volcanoes that underwent Vulcanian to sub-Plinian sized eruptions (VEI 2–4).

Component analysis also provides constraints on eruption style. Most important are the distinctive glass shard layers, and the layers with abundant microlite-bearing clasts, both of which are used to correlate tephras in the two cores. Interestingly, the two layers with distinctive glass shard morphology (ABII-06-77 and ABII-10-73:77 [AGSL1]) occurred at the beginning of, or during, the *quiet* periods (Figure 8). These glass-shard rich, microlite-poor eruptions are also often the thickest deposits in the cores; ABII-06-77 and ABII-10-73:77 are 6- and 5-cm thick, respectively (compared to an average thickness of 3.6 cm) indicating they are the product of bigger eruptions than their microlite-rich counterparts. We infer that these glass shard layers were produced by more explosive eruptions with rapid ascent rates and a deeper, or less degassed source. The microlite-rich deposits (AML1 and AML2), in contrast, occur during periods of increased eruption frequency and are ~2- to 3-cm thick in ABII. Importantly, the other layers in the clusters also comprise microlite-containing grains.

Microlite-rich layers may also provide some insight into the eruption dynamics. In general, the microlite-rich glass has the same major element composition as the microlite-poor glass. The glasses differ in trace element composition, however, as shown in Figure 5. This trace element difference can be explained by degassing-induced crystallization of a eutectic melt and associated enrichment of the relevant incompatible elements (such as Ba; e.g., Scaillet & MacDonald, 2001). The trace element data support our interpretation that microlite-rich layers are produced by eruption of stalled, degassed magma from a shallow system (either a conduit plug or dome). Microlites in other settings have been found to grow in systems ≤4-km depth (e.g., Cashman & McConnell, 2005; Hammer et al., 1999), we infer that this was likely the case at Aluto where a ~4-km deep magma storage is observed (Hutchison, Fusillo, et al., 2016). Moreover, eruption of magma stored at varying depths prior to eruption has been shown to produce simultaneously erupted microlite-rich and microlite-poor textures (e.g., Cashman & McConnell, 2005; Klug & Cashman, 1994); a feature frequently observed in the Aluto tephra layers.

The glass-shard rich eruptions also produced glass with high $TiO_2$ and low $NaO_2$ (Figure 4), which suggests that the deeper, undegassed magmas experienced a different crystallization history than the shallow-stored magma. We hypothesize that the $TiO_2$ variation is controlled by the crystallization (or lack thereof) of aenigmatite, a mineral common in peralkaline settings (e.g., Di Carlo et al., 2010; Gleeson et al., 2017), and which contains 7–10 wt% $TiO_2$. There is some debate as to where aenigmatite appears on the liquidus, although it is likely that it is a late-crystallizing phase, precipitated after $Al_2O_3$ decreases from crystallization of alkali feldspar (Di Carlo et al., 2010; Gleeson et al., 2017; Neave et al., 2012). As $NaO_2$ values are also unusually low, we infer the distinct composition reflects the crystallization of other phases, particularly alkali feldspar.

Maps of Aluto's intracaldera deposits show that pumice cones and obsidian coulées are the most common form of Holocene activity from Aluto (Fontijn et al., 2018; Hutchison, Pyle, et al., 2016). Therefore, it is likely that many of the deposits found in lake sediment cores, particularly the smaller microlite-rich eruptions, are the consequence of this type of activity. Pumice cone eruptions are typically inferred to be sub-Plinian to Strombolian (Houghton et al., 1992; Orsi et al., 1989); we anticipate, based on tephra thicknesses with distance, that activity from Aluto was of a similar size. We do not see any evidence for very large Plinian eruptions in the Holocene, which is important for hazard assessment of the volcano.

We infer Aluto has been quite active and the last burst of activity recorded in the cores was 3,000 years ago. While any estimates of eruption size remain crude, our results provide a reference to which complex, and overlapping terrestrial deposits can be compared. This will in turn enable more realistic interpretations of eruption size in the future.

## 5. Conclusion

We have presented a study of tephra from the Aluto volcano from two lake cores ABII and LLIII. We have revised the age modeling in the cores and applied it to the tephra sequence. Invariance in the major element geochemistry has made the tephra layers from these cores challenging to correlate, and we find we are able to correlate some largely geochemically similar deposits in cores ABII and LLIII through the use of componentry. Many deposits in the core, however, remain uncorrelatable due to the chemical and textural similarities between most eruptions. While typical major elements used for correlations such as $SiO_2$ and FeO are not useful, certain other elements, particularly $TiO_2$ and $NaO_2$ can be used to correlate a minority of tephra layers. These variations, however, have not been sufficient to correlate more than one layer confidently; for this reason, we combined geochemical data with textural information.

Textural data suggest five tephra layer correlations based on the presence and abundance of microlites in the constituent glass, as well as the abundance of glass shards. One glass shard layer was found to coincide with the observed geochemical variations and then independently supported by trace element data. The correlations provide a reference for further tephrostratigraphic study of the volcano, which can be applied to more complex deposits.

The cores also provide a unique opportunity to constrain the volcano's surprisingly lively eruptive history. The ages of the tephras in the core reveal that Aluto has had at least 24 eruptions in the Holocene, which were mostly erupted in bursts of heightened activity, the most recent of which was at ~3.5 ka while the other two occurred at 6.1 and 11 ka. In general, the microlite-rich tephras occurred during the episodes of increased activity, while the glass shard-rich layers were erupted at the end of these periods or during periods of comparative repose.

While we have not made any definitive estimates of eruption size and style due to the lack of spatial data, we infer that the deposits are a consequence of pumice cone and/or dome-building eruptions, which are typically Vulcanian to sub-Plinian in size and style, an observation consistent with other evidence for pumice cones and dome-building activity at Aluto.

## References

Abebe, B., Acocella, V., Korme, T., & Ayalew, D. (2007). Quaternary faulting and volcanism in the Main Ethiopian Rift. *Journal of African Earth Sciences*, *48*(2–3), 115–124. https://doi.org/10.1016/J.JAFREARSCI.2006.10.005

Aspinall, W. P., Auker, M., Hincks, T., Mahony, S., Nadim, F., Pooley, J., et al. (2011). GFDRR, volcano risk study volcano hazard and exposure in GFDRR priority, *NGI report*.

Ayenew, T. (2002). Recent changes in the level of Lake Abiyata, central main Ethiopian Rift. *Hydrological Sciences Journal*, *47*(3), 493–503. https://doi.org/10.1080/02626660209492949

Benvenuti, M., Bonini, M., Tassi, F., Corti, G., Sani, F., Agostini, A., et al. (2013). Holocene lacustrine fluctuations and deep $CO_2$ degassing in the northeastern Lake Langano basin (Main Ethiopian rift). *Journal of African Earth Sciences*, *77*, 1–10. https://doi.org/10.1016/j.jafrearsci.2012.09.001

Benvenuti, M., Carnicelli, S., Belluomini, G., Dainelli, N., di Grazia, S., Ferrari, G. A., et al. (2002). The Ziway-Shala lake basin (main Ethiopian rift, Ethiopia): A revision of basin evolution with special reference to the Late Quaternary. *Journal of African Earth Sciences*, *35*(2), 247–269. https://doi.org/10.1016/S0899-5362(02)00036-2

Bertrand, S., Daga, R., Bedert, R., & Fontijn, K. (2014). Deposition of the 2011–2012 Cordón Caulle tephra (Chile, 40°S) in lake sediments: Implications for tephrochronology and volcanology. *Journal of Geophysical Research: Earth Surface*, *119*, 2555–2573. https://doi.org/10.1002/2014JF003321.Received

Biggs, J., Bastow, I. D., Keir, D., & Lewi, E. (2011). Pulses of deformation reveal frequently recurring shallow magmatic activity beneath the Main Ethiopian Rift. *Geochemistry, Geophysics, Geosystems*, Q0AB10. https://doi.org/10.1029/2011GC003662

Blundy, J., & Cashman, K. (2001). Ascent-driven crystallisation of dacite magmas at Mount St Helens, 1980–1986. *Contributions to Mineralogy and Petrology*, *140*(6), 631–650. https://doi.org/10.1007/s004100000219

Bonadonna, C., Ernst, G. G. J., & Sparks, R. S. J. (1998). Thickness variations and volume estimates of tephra fall deposits: The importance of particle Reynolds number. *Journal of Volcanology and Geothermal Research*, *81*(3–4), 173–187. https://doi.org/10.1016/S0377-0273(98)00007-9

Bonadonna, C., & Houghton, B. F. (2005). Total grain-size distribution and volume of tephra-fall deposits. *Bulletin of Volcanology*, *67*(5), 441–456. https://doi.org/10.1007/s00445-004-0386-2

Brendryen, J., Haflidason, H., & Sejrup, H. P. (2010). Norwegian Sea tephrostratigraphy of marine isotope stages 4 and 5: Prospects and problems for tephrochronology in the North Atlantic region. *Quaternary Science Reviews*, *29*(7–8), 847–864. https://doi.org/10.1016/j.quascirev.2009.12.004

Bronk Ramsey, C. (2008). Deposition models for chronological records. *Quaternary Science Reviews*, *27*(1–2), 42–60. https://doi.org/10.1016/J.QUASCIREV.2007.01.019

Bronk Ramsey, C. (2009). Dealing with outliers and offsets in radiocarbon dating. *Radiocarbon*, *51*(03), 1023–1045. https://doi.org/10.1017/S0033822200034093

Bronk Ramsey, C. B., & Lee, S. (2013). Recent and planned developments of the program OxCal. *Radiocarbon*, *55*(02), 720–730. https://doi.org/10.1017/S0033822200057878

Buckland, H. M., Eychenne, J., Rust, A. C., & Cashman, K. V. (2018). Relating the physical properties of volcanic rocks to the characteristics of ash generated by experimental abrasion. *Journal of Volcanology and Geothermal Research*, *349*, 335–350. https://doi.org/10.1016/j.jvolgeores.2017.11.017

Bursik, M. (1996) Tephra dispersal, in The physics of explosive eruptions, *Geological Society, London, Special Publications*, *145*, pp. 15–144.

Carey, S., & Sparks, R. S. J. (1986). Quantitative models of the fallout and dispersal of tephra from volcanic eruption columns. *Bulletin of Volcanology*, *48*(2-3), 109–125. https://doi.org/10.1007/BF01046546

Cashman, K. V. (2004). In R. S. J. Sparks, & C. J. Hawkesworth (Eds.), *Volatile vontrols on magma ascent and eruption, Geophysical Monograph Series*. https://doi.org/10.1029/150GM10

Cashman, K. V., & McConnell, S. M. (2005). Multiple levels of magma storage during the 1980 summer eruptions of Mount St. Helens, WA. *Bulletin of Volcanology*, *68*(1), 57–75. https://doi.org/10.1007/s00445-005-0422-x

Cashman, K. V., & Rust, A. C. (2016). Volcanic ash: Generation and spatial variations. In *Volcanic ash: Hazard observation* (pp. 5–21). Amsterdam: Elsevier.

Castruccio, A., Clavero, J., Segura, A., Samaniego, P., Roche, O., Le Pennec, J. L., & Droguett, B. (2016). Eruptive parameters and dynamics of the April 2015 sub-Plinian eruptions of Calbuco volcano (southern Chile). *Bulletin of Volcanology*, *78*(9), 62. https://doi.org/10.1007/s00445-016-1058-8

Chalié, F., & Gasse, F. (2002). Late Glacial-Holocene diatom record of water chemistry and lake level change from the tropical East African Rift Lake Abiyata (Ethiopia). *Palaeogeography, Palaeoclimatology, Palaeoecology*, *187*(3-4), 259–283. https://doi.org/10.1016/S0031-0182(02)00480-7

Cioni, R., D'Oriano, C., & Bertagnini, A. (2008). Fingerprinting ash deposits of small scale eruptions by their physical and textural features. *Journal of Volcanology and Geothermal Research*, *177*(1), 277–287. https://doi.org/10.1016/j.jvolgeores.2008.06.003

Cioni, R., Pistolesi, M., Bertagnini, A., Bonadonna, C., Hoskuldsson, A., & Scateni, B. (2014). Insights into the dynamics and evolution of the 2010 Eyjafjallajökull summit eruption (Iceland) provided by volcanic ash textures. *Earth and Planetary Science Letters*, *394*, 111–123. https://doi.org/10.1016/J.EPSL.2014.02.051

Clarke, A. B., Stephens, S., Teasdale, R., Sparks, R. S. J., & Diller, K. (2007). Petrologic constraints on the decompression history of magma prior to Vulcanian explosions at the Soufrière Hills volcano, Montserrat. *Journal of Volcanology and Geothermal Research*, *161*(4), 261–274. https://doi.org/10.1016/J.JVOLGEORES.2006.11.007

Coltelli, M., Del Carlo, P., & Vezzoli, L. (1998). Discovery of a Plinian basaltic eruption of roman age at Etna volcano, Italy. *Geology*, *26*(12), 1095–1098. https://doi.org/10.1130/0091-7613(1998)026<1095:DOAPBE>2.3.CO;2

Connor, C. B., Sparks, R. S. J., Mason, R. M., Bonadonna, C., & Young, S. R. (2003). Exploring links between physical and probabilistic models of volcanic eruptions: The Soufrière Hills volcano, Montserrat. *Geophysical Research Letters*, *30*(13), 1701. https://doi.org/10.1029/2003GL017384

Corti, G. (2009). Continental rift evolution: From rift initiation to incipient break-up in the Main Ethiopian Rift, East Africa. *Earth-Science Reviews*, *96*(1–2), 1–53. https://doi.org/10.1016/j.earscirev.2009.06.005

Dellino, P., & La Volpe, L. (1996). Image processing analysis in reconstructing fragmentation and transportation mechanisms of pyroclastic deposits. The case of Monte Pilato-Rocche Rosse eruptions, Lipari (Aeolian islands, Italy). *Journal of Volcanology and Geothermal Research*, *71*(1), 13–29. https://doi.org/10.1016/0377-0273(95)00062-3

Di Carlo, I., Rotolo, S. G., Scaillet, B., Buccheri, V., & Pichavant, M. (2010). Phase equilibrium constraints on pre-eruptive conditions of recent felsic explosive volcanism at Pantelleria Island, Italy. *Journal of Petrology*, *51*(11), 2245–2276. https://doi.org/10.1093/petrology/egq055

Di Paola, G. M. (1972). The Ethiopian Rift Valley (between 700′ and 840′ lat. north). *Bulletin Volcanologique*, *36*(4), 517–560. https://doi.org/10.1007/BF02599823

Di Roberto, A., Smedile, A., Del Carlo, P., De Martini, P. M., Iorio, M., Petrelli, M., et al. (2018). Tephra and cryptotephra in a ~ 60,000-year-old lacustrine sequence from the Fucino Basin: New insights into the major explosive events in Italy. *Bulletin of Volcanology*, *80*(3), 20. https://doi.org/10.1007/s00445-018-1200-x

Ebinger, C., & Casey, M. (2001). Continental breakup in magmatic provinces: An Ethiopian example. *Geology*, *29*(6), 527–530.

Fierstein, J. (2007). Explosive eruptive record in the Katmai region, Alaska peninsula: An overview. *Bulletin of Volcanology*, *69*(5), 469–509. https://doi.org/10.1007/s00445-006-0097-y

Fierstein, J., & Nathenson, M. (1992). Another look at the calculation of fallout tephra volumes. *Bulletin of Volcanology*, *54*(2), 156–167. https://doi.org/10.1007/BF00278005

Fontijn, K., Costa, F., Sutawidjaja, I., Newhall, C. G., & Herrin, J. S. (2015). A 5000-year record of multiple highly explosive mafic eruptions from Gunung Agung (Bali, Indonesia): Implications for eruption frequency and volcanic hazards. *Bulletin of Volcanology*, *77*(7), 59. https://doi.org/10.1007/s00445-015-0943-x

Fontijn, K., Ernst, G. G. J., Bonadonna, C., Elburg, M. A., Mbede, E., & Jacobs, P. (2011). The 4-ka Rungwe Pumice (South-Western Tanzania): A wind-still Plinian eruption. *Bulletin of Volcanology*, *73*(9), 1353–1368. https://doi.org/10.1007/s00445-011-0486-8

Fontijn, K., McNamara, K., Tadesse, A. Z., Pyle, D. M., Dessalegn, F., Hutchison, W., et al. (2018). Contrasting styles of post-caldera volcanism along the Main Ethiopian Rift: Implications for contemporary volcanic hazards. *Journal of Volcanology and Geothermal Research*, *356*, 90–113. https://doi.org/10.1016/j.jvolgeores.2018.02.001

Fontijn, K., Rawson, H., van Daele, M., Moernaut, J., Abarzúa, A. M., Heirman, K., et al. (2016). Synchronisation of sedimentary records using tephra: A postglacial tephrochronological model for the Chilean Lake District. *Quaternary Science Reviews*, *137*, 234–254. https://doi.org/10.1016/J.QUASCIREV.2016.02.015

Gasse, E., & Street, F. A. (1978). Late Quaternary Lake-level fluctuations and environments of the northern Rift valley and Afar region (Ethiopia and Djibouti). *Palaeogeography, Palaeoclimatology, Palaeoecology*, *24*(4), 279–325. https://doi.org/10.1016/0031-0182(78)90011-1

Geschwind, C. H., & Rutherford, M. J. (1995). Crystallization of microlites during magma ascent: The fluid mechanics of 1980-1986 eruptions at mount St Helens. *Bulletin of Volcanology*, *57*(5), 356–370. https://doi.org/10.1007/BF00301293

Gianelli, G., & Teklemariam, M. (1993). Water-rock interaction processes in the Aluto-Langano geothermal field (Ethiopia). *Journal of Volcanology and Geothermal Research*, *56*(4), 429–445. https://doi.org/10.1016/0377-0273(93)90007-E

Gibert, E., Travi, Y., Massault, M., Chernet, T., Barbecot, F., & Laggoun-Defarge, F. (1999). Comparing carbonate and organic Ams-^{14}C ages in Lake Abiyata sediments (Ethiopia): Hydrochemistry and paleoenvironmental implications. *Radiocarbon*, *41*(03), 271–286. https://doi.org/10.1017/S0033822200057131

Gibert, E., Travi, Y., Massault, M., Tiercelin, J.-J., & Chernet, T. (2002). Ams-14C chronology of a lacustrine sequence from Lake Langano (main Ethiopian rift): Correction and validation steps in relation with volcanism, Lake water and carbon balances. *Radiocarbon*, *44*(01), 75–92. https://doi.org/10.1017/S0033822200064699

Gleeson, M. L. M., Stock, M. J., Pyle, D. M., Mather, T. A., Hutchison, W., Yirgu, G., & Wade, J. (2017). *Constraining magma storage conditions at a restless volcano in the Main Ethiopian Rift using phase equilibria models, Journal of Volcanology and Geothermal Research*. doi: https://doi.org/10.1016/j.jvolgeores.2017.02.026, (Vol. 337, pp. 44–61).

Hammer, J. E., Cashman, K. V., Hoblitt, R. P., & Newman, S. (1999). Degassing and microlite crystallization during pre-climactic events of the 1991 eruption of Mt. Pinatubo, Philippines. *Bulletin of Volcanology*, *60*(5), 355–380. https://doi.org/10.1007/s004450050238

Henderson, C. M. B., & Pierozynski, W. J. (2012). An experimental study of Sr, Ba and Rb partitioning between alkali feldspar and silicate liquid in the system nepheline–kalsilite–quartz at 0.01 GPa P(H$_2$O): a revisitation and reassessment. *Mineralogical Magazine*, *76*(1), 157–190. https://doi.org/10.1180/minmag.2012.076.1.157

Hildreth, W., & Drake, R. E. (1992). Volcán Quizapu, Chilean Andes. *Bulletin of Volcanology*, *54*(2), 93–125. https://doi.org/10.1007/BF00278002

Ho, C.-H. (1996). Volcanic time-trend analysis. *Journal of Volcanology and Geothermal Research*, *74*(3–4), 171–177. https://doi.org/10.1016/S0377-0273(96)00057-1

Houghton, B. F., Weaver, S. D., Wilson, C. J. N., & Lanphere, M. A. (1992). Evolution of a quaternary peralkaline volcano: Mayor Island, New Zealand. *Journal of Volcanology and Geothermal Research*, *51*(3), 217–236. https://doi.org/10.1016/0377-0273(92)90124-V

Hutchison, W., Biggs, J., Mather, T. A., Pyle, D. M., Lewi, E., Yirgu, G., et al. (2016). Causes of unrest at silicic calderas in the East African rift: New constraints from InSAR and soil-gas chemistry at Aluto volcano, Ethiopia. *Geochemistry, Geophysics, Geosystems*, *17*(8), 3008–3030. https://doi.org/10.1002/2016GC006395

Hutchison, W., Fusillo, R., Pyle, D. M., Mather, T. A., Blundy, J. D., Biggs, J., et al. (2016). A pulse of mid-Pleistocene rift volcanism in Ethiopia at the dawn of modern humans. *Nature Communications*, *7*, 13,192. https://doi.org/10.1038/ncomms13192

Hutchison, W., Pyle, D. M., Mather, T. A., Yirgu, G., Biggs, J., Cohen, B. E., et al. (2016). The eruptive history and magmatic evolution of Aluto volcano: New insights into silicic peralkaline volcanism in the Ethiopian rift. *Journal of Volcanology and Geothermal Research*, *328*, 9–33. https://doi.org/10.1016/j.jvolgeores.2016.09.010

Jochum, K. P., Weis, U., Schwager, B., Stoll, B., Wilson, S. A., Haug, G. H., et al. (2016). Reference Values Following ISO Guidelines for Frequently Requested Rock Reference Materials. *Geostandards and Geoanalytical Research*, *40*(3), 333–350. https://doi.org/10.1111/j.1751-908X.2015.00392.x

Jones, T. J., McNamara, K., Eychenne, J., Rust, A. C., Cashman, K. V., Scheu, B., & Edwards, R. (2016). Primary and secondary fragmentation of crystal-bearing intermediate magma. *Journal of Volcanology and Geothermal Research*, *327*, 70–83. https://doi.org/10.1016/j.jvolgeores.2016.06.022

Kalnay, E., Kanamitsu, M., Kistler, R., Collins, W., Deaven, D., Gandin, L., et al. (1996). The NCEP/NCAR 40-year reanalysis project. *Bulletin of the American Meteorological Society*, *77*(3), 437–471. https://doi.org/10.1175/1520-0477(1996)077<0437:TNYRP>2.0.CO;2

Keir, D., Bastow, I. D., Corti, G., Mazzarini, F., & Rooney, T. O. (2015). The origin of along-rift variations in faulting and magmatism in the Ethiopian rift. *Tectonics*, *34*, 464–477. https://doi.org/10.1002/2014TC003698.Received

Klug, C., & Cashman, K. V. (1994). Vesiculation of May 18, 1980, Mount St. Helens magma. *Geology*, *22*(5), 468–472. https://doi.org/10.1130/0091-7613(1994)022%3C0468:VOMMSH%3E2.3.CO

Kuehn, S. C., & Foit, F. F. (2006). Correlation of widespread Holocene and Pleistocene tephra layers from Newberry Volcano, Oregon, USA, using glass compositions and numerical analysis. *Quaternary International*, *148*(1), 113–137. https://doi.org/10.1016/j.quaint.2005.11.008

Kuehn, S. C., & Negrini, R. M. (2010). A 250 k.y. record of Cascade arc pyroclastic volcanism from late Pleistocene lacustrine sediments near Summer Lake, Oregon, USA. *Geosphere*, *6*(4), 397. https://doi.org/10.1130/GES00515.1

Lamb, A. L., Leng, M. J., Lamb, H. F., Telford, R. J., & Mohammed, M. U. (2002). Climatic and non-climatic effects on the $\delta^{18}$O and $\delta^{13}$C compositions of Lake Awassa, Ethiopia, during the last 6.5 ka. *Quaternary Science Reviews*, *21*(20–22), 2199–2211. https://doi.org/10.1016/S0277-3791(02)00087-2

Le Turdu, C., Tiercelin, J.-J., Gibert, E., Travi, Y., Lezzar, K.-E., Richert, J.-P., et al. (1999). The Ziway–Shala lake basin system, Main Ethiopian Rift: Influence of volcanism, tectonics, and climatic forcing on basin formation and sedimentation. *Palaeogeography, Palaeoclimatology, Palaeoecology*, *150*(3–4), 135–177. https://doi.org/10.1016/S0031-0182(98)00220-X

Legros, F. (2000). Minimum volume of a tephra fallout deposit estimated from a single isopach. *Journal of Volcanology and Geothermal Research*, *96*(1-2), 25–32. https://doi.org/10.1016/S0377-0273(99)00135-3

Liu, E. J., Cashman, K. V., Rust, A. C., & Gislason, S. R. (2015). The role of bubbles in generating fine ash during hydromagmatic eruptions. *Geology*, *43*(3), 239–242. https://doi.org/10.1130/G36336.1

Liu, E. J., Cashman, K. V., Rust, A. C., & Höskuldsson, A. (2017). Contrasting mechanisms of magma fragmentation during coeval magmatic and hydromagmatic activity: The Hverfjall fires fissure eruption, Iceland. *Bulletin of Volcanology*, *79*(10), 68. https://doi.org/10.1007/s00445-017-1150-8

Liu, E. J., Oliva, M., Antoniades, D., Giralt, S., Granados, I., Pla-Rabes, S., et al. (2016). Expanding the tephrostratigraphical framework for the South Shetland Islands, Antarctica, by combining compositional and textural tephra characterisation. *Sedimentary Geology*, *340*, 49–61. https://doi.org/10.1016/J.SEDGEO.2015.08.002

Lloyd, R., Biggs, J., Wilks, M., Nowacki, A., Kendall, J.-M., Ayele, A., et al. (2018). Evidence for cross rift structural controls on deformation and seismicity at a continental rift caldera. *Earth and Planetary Science Letters*, *487*, 190–200. https://doi.org/10.1016/J.EPSL.2018.01.037

Lowe, D. J. (2011). Quaternary geochronology tephrochronology and its application: A review. *Quaternary Geochronology*, *6*(2), 107–153. https://doi.org/10.1016/j.quageo.2010.08.003

Martin-Jones, C. M., Lane, C. S., G Pearce, N. J., Smith, V. C., Lamb, H. F., Schaebitz, F., et al. (2017). Recurrent explosive eruptions from a high-risk Main Ethiopian Rift volcano throughout the Holocene. *Geology*, *45*, 1127–1130. https://doi.org/10.1130/G39594.1

Melnik, O., & Sparks, R. S. J. (1999). Nonlinear dynamics of lava dome extrusion. *Nature*, *402*(6757), 37–41. https://doi.org/10.1038/46950

Miwa, T., Geshi, N., & Shinohara, H. (2013). Temporal variation in volcanic ash texture during a vulcanian eruption at the Sakurajima volcano, Japan. *Journal of Volcanology and Geothermal Research*, *260*, 80–89. https://doi.org/10.1016/J.JVOLGEORES.2013.05.010

Miyabuchi, Y., Hanada, D., Niimi, H., & Kobayashi, T. (2013). Stratigraphy, grain-size and component characteristics of the 2011 Shinmoedake eruption deposits, Kirishima volcano, Japan. *Journal of Volcanology and Geothermal Research*, *258*, 31–46. https://doi.org/10.1016/J.JVOLGEORES.2013.03.027

Mohr, P., Mitchell, J. G., & Raynolds, R. G. H. (1980). Quaternary volcanism and faulting at O'A caldera, central Ethiopian rift. *Bulletin Volcanologique*, *43*(1), 173–189. https://doi.org/10.1007/BF02597619

Mohr, P. A. (1966). Chahbi volcano (Ethiopia). *Bulletin Volcanologique*, *29*(1), 797–815. https://doi.org/10.1007/BF02597195

Mohr, P. A. (1971). Ethiopian rift and plateaus: Some volcanic petrochemical differences. *Journal of Geophysical Research*, *76*(8), 1967–1984. https://doi.org/10.1029/JB076i008p01967

Mohr, P. A., & Wood, C. A. (1976). Volcano spacings and lithospheric attenuation in the eastern rift of Africa. *Earth and Planetary Science Letters*, *33*(1), 126–144. https://doi.org/10.1016/0012-821X(76)90166-7

Moreno, P. I., Alloway, B. V., Villarosa, G., Outes, V., Henríquez, W. I., De Pol-Holz, R., & Pearce, N. J. G. (2015). A past-millennium maximum in postglacial activity from Volcán Chaitén, southern Chile. *Geology*, *43*(1), 47–50. https://doi.org/10.1130/G36248.1

Nakada, S., Nagai, M., Kaneko, T., Suzuki, Y., & Maeno, F. (2013). The outline of the 2011 eruption at Shinmoe-dake (Kirishima), Japan. *Earth, Planets and Space*, *65*(6), 475–488. https://doi.org/10.5047/eps.2013.03.016

Neave, D. A., Fabbro, G., Herd, R. A., Petrone, C. M., & Edmonds, M. (2012). Melting, differentiation and degassing at the pantelleria volcano, Italy. *Journal of Petrology*, *53*(3), 637–663. https://doi.org/10.1093/petrology/egr074

Noguchi, S., Toramaru, A., & Shimano, T. (2006). Crystallization of microlites and degassing during magma ascent: Constraints on the fluid mechanical behavior of magma during the Tenjo eruption on Kozu Island, Japan. *Bulletin of Volcanology*, *68*(5), 432–449. https://doi.org/10.1007/s00445-005-0019-4

Orsi, G., Ruvo, L., & Scarpati, C. (1989). The Serra della Fastuca tephra at Pantelleria: Physical parameters for an explosive eruption of per-alkaline magma. *Journal of Volcanology and Geothermal Research*, *39*(1), 55–60. https://doi.org/10.1016/0377-0273(89)90020-6

Placzek, C., Quade, J., Rech, J. A., Patchett, P. J., & Pe, C. (2009). Quaternary Geochronology Geochemistry, chronology and stratigraphy of Neogene tuffs of the Central Andean region. *Quaternary Geochronology*, *4*, 22–36. https://doi.org/10.1016/j.quageo.2008.06.002

Pyle, D. M. (1989). The thickness, volume and grainsize of tephra fall deposits. *Bulletin of Volcanology*, *51*(1), 1–15. https://doi.org/10.1007/BF01086757

Rapprich, V., Žáček, V., Verner, K., Erban, V., Goslar, T., Bekele, Y., et al. (2016). Wendo Koshe Pumice: The latest Holocene silicic explosive eruption product of the Corbetti volcanic system (southern Ethiopia). *Journal of Volcanology and Geothermal Research*, *310*, 159–171. https://doi.org/10.1016/J.JVOLGEORES.2015.12.008

Rawson, H., Naranjo, J. A., Smith, V. C., Fontijn, K., Pyle, D. M., Mather, T. A., & Moreno, H. (2015). The frequency and magnitude of post-glacial explosive eruptions at Volcán Mocho-Choshuenco, southern Chile. *Journal of Volcanology and Geothermal Research*, *299*, 103–129. https://doi.org/10.1016/J.JVOLGEORES.2015.04.003

Reimer, P. J., Bard, E., Bayliss, A., Beck, J. W., Blackwell, P. G., Ramsey, C. B., et al. (2013). IntCal13 and Marine13 radiocarbon age calibration curves 0–50,000 years cal BP. *Radiocarbon*, *55*(04), 1869–1887. https://doi.org/10.2458/azu_js_rc.55.16947

Rooney, T. O., Furman, T., Yirgu, G., & Ayalew, D. (2005). Structure of the Ethiopian lithosphere: Xenolith evidence in the main Ethiopian rift. *Geochimica et Cosmochimica Acta*, *69*(15), 3889–3910. https://doi.org/10.1016/j.gca.2005.03.043

Rose, W. I., & Chesner, C. A. (1987). Dispersal of ash in the great Toba eruption, 75 ka. *Geology*, *15*(10), 913–917. https://doi.org/10.1130/0091-7613(1987)15<913:DOAITG>2.0.CO;2

Samrock, F., Kuvshinov, A., Bakker, J., Jackson, A., & Fisseha, S. (2015). 3-D analysis and interpretation of magnetotelluric data from the Aluto-Langano geothermal field, Ethiopia. *Geophysical Journal International*, *202*(3), 1923–1948. https://doi.org/10.1093/gji/ggv270

Scaillet, B., & MacDonald, R. A. Y. (2001). Phase relations of peralkaline silicic magmas and petrogenetic implications. *Journal of Petrology*, *42*(4), 825–845. https://doi.org/10.1093/petrology/42.4.825

Scarpati, C., Sparice, D., & Perrotta, A. (2014). A crystal concentration method for calculating ignimbrite volume from distal ash-fall deposits and a reappraisal of the magnitude of the Campanian ignimbrite. *Journal of Volcanology and Geothermal Research*, *280*, 67–75. https://doi.org/10.1016/J.JVOLGEORES.2014.05.009

Schindelin, J., Arganda-Carreras, I., Frise, E., Kaynig, V., Longair, M., Pietzsch, T., et al. (2012). Fiji: An open-source platform for biological-image analysis. *Nature Methods*, *9*(7), 676–682. https://doi.org/10.1038/nmeth.2019

Schmincke, H. U. (1974). Volcanological aspects of peralkaline silicic welded ash-flow tuffs. *Bulletin Volcanologique*, *38*(2), 594–636. https://doi.org/10.1007/BF02596900

Shane, P., Black, T., Eggins, S., & Westgate, J. (1998). Late Miocene marine tephra beds: Recorders of rhyolitic volcanism in North Island, New Zealand. *New Zealand Journal of Geology and Geophysics*, *41*(2), 165–178. https://doi.org/10.1080/00288306.1998.9514801

Shane, P., & Smith, I. (2000). Geochemical fingerprinting of basaltic tephra deposits in the Auckland volcanic field. *New Zealand Jounrla of Geology and Geophysics*, *43*(4), 569–577. https://doi.org/10.1080/00288306.2000.9514909

Sheldrake, T. E., Sparks, R. S. J., Cashman, K. V., Wadge, G., & Aspinall, W. P. (2016). Similarities and differences in the historical records of lava dome-building volcanoes: Implications for understanding magmatic processes and eruption forecasting. *Earth-Science Reviews*, *160*, 240–263. https://doi.org/10.1016/J.EARSCIREV.2016.07.013

Smith, V. C., Matthews, N. E., Westgate, J. A., Petraglia, M. D., Haslam, M., Lane, C. S., et al. (2011). Geochemical fingerprinting of the widespread Toba tephra using biotite compositions. *Quaternary International*, *246*(1–2), 97–104. https://doi.org/10.1016/J.QUAINT.2011.05.012

Sparks, R. S. J. (1997). Causes and consequences of pressurisation in lava dome eruptions. *Earth and Planetary Science Letters*, *150*(3–4), 177–189. https://doi.org/10.1016/S0012-821X(97)00109-X

Swanson, S. E., Naney, M. T., Westrich, H. R., & Eichelberger, J. C. (1989). Crystallization history of obsidian dome, Inyo Domes, California. *Bulletin of Volcanology*, *51*(3), 161–176. https://doi.org/10.1007/BF01067953

Szramek, L., Gardner, J. E., & Larsen, J. (2006). Degassing and microlite crystallization of basaltic andesite magma erupting at Arenal volcano, Costa Rica. *Journal of Volcanology and Geothermal Research*, *157*(1–3), 182–201. https://doi.org/10.1016/j.jvolgeores.2006.03.039

Teklemariam, M., Battaglia, S., Gianelli, G., & Ruggieri, G. (1996). Hydrothermal alteration in the Aluto-Langano geothermal field, Ethiopia. *Geothermics*, *25*(6), 679–702. https://doi.org/10.1016/S0375-6505(96)00019-3

Thompson, R., Bradshaw, R. H. W., & Whitley, J. E. (1986). The distribution of ash in Icelandic lake sediments and the relative importance of mixing and erosion processes. *Journal of Quaternary Science*, *1*(1), 3–11. https://doi.org/10.1002/jqs.3390010102

Trua, T., Deniel, C., & Mazzuoli, R. (1999). Crustal control in the genesis of Plio-Quaternary bimodal magmatism of the Main Ethiopian Rift (MER): Geochemical and isotopic (Sr, Nd, Pb) evidence. *Chemical Geology*, *155*(3–4), 201–231. https://doi.org/10.1016/S0009-2541(98)00174-0

Tryon, C. A., Roach, N. T., & Logan, M. A. V. (2008). The Middle Stone Age of the northern Kenyan Rift: Age and context of new archaeological sites from the Kapedo Tuffs. *Journal of Human Evolution*, *55*(4), 652–664. https://doi.org/10.1016/j.jhevol.2008.03.008

Vogel, H., Wagner, B., & Rose, P. (2010). A paleoclimate record with tephrochronological age control for the last glacial-interglacial cycle from Lake Ohrid, Albania and Macedonia. *Journal of Paleolimnology*, *44*(1), 295–310. https://doi.org/10.1007/s10933-009-9404-x

Wei, H., Sparks, R. S. J., Liu, R., Fan, Q., Wang, Y., Hong, H., et al. (2003). Three active volcanoes in China and their hazards. *Journal of Asian Earth Sciences*, *21*(5), 515–526. https://doi.org/10.1016/S1367-9120(02)00081-0

Wilks, M., Kendall, J.-M., Nowacki, A., Biggs, J., Wookey, J., Birhanu, Y., et al. (2017). Seismicity associated with magmatism, faulting and hydrothermal circulation at Aluto volcano, main Ethiopian rift. *Journal of Volcanology and Geothermal Research*, *340*, 52–67. https://doi.org/10.1016/J.JVOLGEORES.2017.04.003

WoldeGabriel, G., Aronson, J. L., & Walter, R. C. (1990). Geology, geochronology, and rift basin development in the central sector of the main Ethiopia rift. *Bulletin of the Geological Society of America*, *102*(4), 439–458. https://doi.org/10.1130/0016-7606(1990)102<0439:GGARBD>2.3.CO;2

World Bank (2007). Population and housing census 2007 report, Oromiya, *Part I: Population Size and Characteristics*. Available at: http://microdata.worldbank.org/index.php/catalog/2747

Wright, H. M. N., Cashman, K. V., Mothes, P. A., Hall, M. L., Ruiz, A. G., & Le Pennec, J. (2012). Estimating rates of decompression from textures of erupted ash particles produced by 1999–2006 eruptions of Tungurahua volcano, Ecuador. *Geology*, *40*(7), 619–622. https://doi.org/10.1130/G32948.1

Wulf, S., Kraml, M., Brauer, A., Keller, J., & Negendank, J. F. W. (2004). Tephrochronology of the 100 ka lacustrine sediment record of Lago Grande di Monticchio (southern Italy). *Quaternary International*, *122*(1 SPEC. ISS), 7–30. https://doi.org/10.1016/j.quaint.2004.01.028

Zinabu, G. M., Kebede-Westhead, E., & Desta, Z. (2002). Long-term changes in chemical features of waters of seven Ethiopian rift-valley lakes. *Hydrobiologia*, *477*(1/3), 81–91. https://doi.org/10.1023/A:1021061015788